

AN ABSTRACT OF THE THESIS OF

Jeremy Matthew Flowers for the degree of Master of Science in Mechanical Engineering presented on March 24, 2015.

Title: Design and Testing of an Integrated Wildlife-Wind Turbine Interactions Detection System.

Abstract approved:

Roberto Albertani

Bird and bat mortalities caused by interactions with wind turbines is a critical concern that requires addressing for conservation purposes. Deploying a low cost sensor array will be instrumental during site permitting, conducting impact assessments of existing wind farms, and assessing efficacy of wildlife mortality mitigation or wildlife deterrent technologies. While carcass surveys are the standard method for measuring wildlife mortality for onshore sites, the method is inadequate due to factors such as carcass removal. For offshore wind turbines, there is no industry adopted method for evaluating wildlife mortality. A near-real-time detection system could quantify wildlife interaction rates of both onshore and offshore wind facilities. This US Department of Energy funded project covers the development and testing of a multi-sensor instrumentation package capable of detecting avian and bat interactions with the blades, nacelle, and tower of a wind turbine. The onboard, integrated sensor package includes contact microphones, accelerometers, visual and infrared spectrum cameras

as well as bioacoustic monitoring. Infrared or visual image recording are necessary for event confirmation and taxonomic classification. Simulated impacts using tennis balls were successfully recorded in tests on the wind turbines at the North American Wind Research and Training Center, Mesalands Community College, New Mexico and the National Wind Technology Center, National Renewable Energy Lab, Colorado, proving the system's operability. Accelerometers were shown to be the more reliable sensor while contact microphones were shown to be the more sensitive sensor. Results also revealed the requirement of mounting both sensors on each blade for reliable detection. A 1296 x 972 pixel resolution was recognized as an acceptable camera setting for the focal length scale to perform species identification on a medium sized sea bird. Acceptable camera positions were found on the nacelle and on the tower near the ground with both looking at the lower blade sweep area. A custom computer was assembled to handle the network data. The data volume requiring manual review was reduced by incorporating event-based triggering ring buffers into the system's software structure.

The system will be capable of long term, unattended deployment by improving the automatic event detection algorithm and robustness of the system's software architecture.

©Copyright by Jeremy Matthew Flowers
March 24, 2015
All Rights Reserved

Design and Testing of an Integrated Wildlife-Wind Turbine Interactions Detection
System

by
Jeremy Matthew Flowers

A THESIS

submitted to

Oregon State University

in partial fulfillment of
the requirements for the
degree of

Master of Science

Presented March 24, 2015
Commencement June 2015

Master of Science thesis of Jeremy Matthew Flowers presented on March 24, 2015

APPROVED:

Major Professor, representing Mechanical Engineering

Head of the School of Mechanical, Industrial, and Manufacturing Engineering

Dean of the Graduate School

I understand that my thesis will become part of the permanent collection of Oregon State University libraries. My signature below authorizes release of my thesis to any reader upon request.

Jeremy Matthew Flowers, Author

ACKNOWLEDGEMENTS

I would like to thank my academic adviser, Dr. Roberto Albertani, for providing me the opportunity to continue my studies as a graduate student at Oregon State University. I really appreciate your patience and advice. Thank you for training me in the formal research process. I learned a variety of valuable skill sets through your direct guidance: instrumentation, field test planning and data collection, signal processing, and data analysis.

To the United States tax payers and the Department of Energy, for providing the funding for this grant and valuing the potential of offshore wind energy.

To my research colleagues, Trevor Harrison, Dr. Robert Suryan, Dr. Brian Polagye, Congcong Hu and Josh Wilcox, it been an honor working with you on this project.

A special thank you to Will Beattie, for working alongside of me and taking on the enormous task of coding the detection system. I am indebted greatly to you both for your time and your knowledge.

I am grateful for the outstanding assistance that the staff at North American Wind Research and Training Center, Mesalands Community College and National Wind Technology Center, NREL gave when the research team was performing field tests at the sites. They played a tremendous role in the success the team achieved in executing these two system field tests. Special thanks to Jim Morgan and Lee Jay Fingersh for working with us to coordinate the trips.

To Brian Jenson, Gary Borntrager, and Darin Kempton at the MIME Machining and Product Realization Laboratory, for helping me throughout the project to solve all of my challenging manufacturing tasks.

To Lynn Paul, for guiding me through all of MIME and OSU's academic requirements and for helping me not get too overwhelmed in my last term of school.

To my fellow lab colleagues, for helping me solve different research problems.

Thank you to Dr. Bruce Dugger and Theodore Squires, for allowing me take pictures of taxidermy birds and bats in the OSU's Department of Fisheries and Wildlife's Birds, Mammals, and Fishes Collections.

Thank you to Aimee Clark at the Graduate Writing Center, for helping me overcome my writing block and for meeting with me twice weekly to work on my thesis with me.

I also appreciate my committee members, Dr. Bryony DuPont, Dr. Rob Stone, and Anita Azrenko, for volunteering their time and for providing valuable feedback.

Finally, I would like to thank my family and friends. I love you all, and I would not have achieved this personal dream without your support. Thank you Dad for inspiring me to be an inventor through your workshop tinkering. Mom, thank you for your nurturing love during the good and bad times of my education.

TABLE OF CONTENTS

	<u>Page</u>
1. Introduction	1
2. Background and Literature Review	5
2.1. Environmental Monitoring Techniques for Wind Turbines.....	6
2.2. Bird and Bat Monitoring Techniques.....	6
2.2.1. Thermal Animal Detection System.....	6
2.2.2. WT-Bird.....	7
2.2.3. DTBird	8
2.3. Wireless Accelerometer Evaluation Studies	8
2.4. Species of Interest	8
2.5. Wavelet Analysis.....	13
2.6. Ring Buffer.....	13
3. Component Selection and System Design.....	15
3.1. Component Selection	15
3.1.1. Triggering Computer and Labview Programming.....	15
3.1.2. Local Network Design	18
3.1.3. Smart Camera.....	20
3.1.4. Vibrational Sensors.....	22
3.1.5. Bioacoustic Microphones.....	25
3.1.6. Optical Camera Node.....	26
3.1.7. Compressed Air Cannon	28
3.2. System Design.....	28
3.2.1. Mesalands Visit System Design.....	28
3.2.2. NREL 2 Visit System Design	30
4. Methodology.....	34
4.1. Experimental Procedures.....	34
4.1.1. Lab Testing and Validation.....	34
4.1.2. Mesalands Community College Field Testing.....	36
4.1.3. NREL Field Testing.....	43
4.1.4. Testing of the Camera Settings	48
4.2. Theoretical Methods.....	52
4.2.1. Field data examination.....	52

TABLE OF CONTENTS (Continued)

	<u>Page</u>
4.2.2. Image Pixel Simulator.....	56
4.2.3. Application of the Wavelet Algorithm	60
5. Field Tests Results and Discussion	62
5.1. Mesalands.....	62
5.1.1. Lessons from the Wireless Communication Design.....	62
5.1.2. Vibrational Sensors.....	63
5.1.3. Camera Placement	72
5.2. Newport Image Evaluation for Camera Settings.....	74
6. Conclusions and Future Work	76
6.1. Conclusions	76
6.2. Future Work	78
Bibliography	79

LIST OF FIGURES

<u>Figure</u>	<u>Page</u>
Figure 2.1 Marbled murrelet (top), cassin's auklet (second from top), western gull (third from top), and laysan albatross (bottom).	10
Figure 2.2 Marbled murrelet (top), cassin's auklet (second from top), western gull (third from top), and laysan albatross (bottom).	10
Figure 2.3 Western gull (top), and laysan albatross (bottom).....	11
Figure 2.4 Marbled murrelet (top), cassin's auklet (bottom).	11
Figure 2.5 Siver-hared bat (otp) and hoary bat (bottom).....	12
Figure 2.6 Ring buffer architecture and event detection.....	14
Figure 3.1 A diagram of the communication between Labview programs.....	18
Figure 3.2 Wiring diagram of the equipment placement at the Mesalands visit.	29
Figure 3.3 Diagram showing the equipment placement on the wind turbine for the Mesalands testing.....	30
Figure 3.4 Wiring diagram of the equipment placement for the NREL 2 visit.	32
Figure 3.5 Diagram showing the equipment placement on the wind turbine for the NREL 2 visit.	33
Figure 4.1 (T) raw signal from accelerometer attached to shaker (B) wavelet analysis of signal.....	35
Figure 4.2 An image of the sensors mounted to the blades.	37
Figure 4.3 Vibrational sensors mounted to the blade.	38
Figure 4.4 The installation from the top of the hub.	38
Figure 4.5 Air cannon.	40
Figure 4.6 Computer and wireless receivers setup in the field	41
Figure 4.7 A reconstruction of the computer-receiver connections in the field	41
Figure 4.8 An evaluated camera location.	43
Figure 4.9 Taking images from the Nacelle.....	43
Figure 4.10 The microphone and the accelerometer mounted to the CART 3 blade. .	44
Figure 4.11 The accelerometer (left) and the contact microphone external battery box.....	44
Figure 4.12 The sensors being installed onto the blades from a man lift.	45
Figure 4.13 The smart cameras on top of the nacelle looking to the lower blade quadrant.....	45

LIST OF FIGURES (Continued)

<u>Figure</u>	<u>Page</u>
Figure 4.14 The front and the top view of the weatherproof receiver case for NREL 2.....	47
Figure 4.15 Silver-haired bat Wings extended.....	49
Figure 4.16 Using two consecutive frames, two field of view and two bird distances from the camera are compared.....	50
Figure 4.17 The impact amplitude calculation is illustrated on a blade mallet hit..	54
Figure 4.18 The coverage of the rotor blade sweep area by field of view captured by camera one (blue) and two (green).	59
Figure 4.19 Raw signal and wavelet analysis for a microphone recording.	61
Figure 4.20 Raw signal and wavelet analysis for an accelerometer recording.	61
Figure 5.1 Raw signal plots from accelerometer (top) and contact microphone (bottom).....	63
Figure 5.2 An accelerometer recording of a startup.	64
Figure 5.3 An accelerometer recording of a shutdown.	65
Figure 5.4 A blade mallet strikes with the observed response by the microphone (first) and the accelerometer (second) pair.	66
Figure 5.5 Measured reaction to a tennis ball impact for all three microphone-accelerometer pairs, Microphone (1st, 3rd, 5th), Accelerometer (2nd, 4th, 6th).....	66
Figure 5.6 The location breakdown for the 33 tennis ball impacts.....	67
Figure 5.7 With one microphone and one accelerometer mounted to each of the three blades, the chart breaks down of how many of those sensors detected each simulated impact.....	68
Figure 5.8 The number of visually detected impacts broken down by blade for each sensor type.	70
Figure 5.9 Two examples of the camera results from the ground.	72
Figure 5.10 Camera on the nacelle looking up the blade length.....	73
Figure 5.11 Camera at the back of the nacelle looking up at the blade tip.	74
Figure 5.12 The 102 m image taken with 30 mm FL zoomed in on the focal point. ..	75
Figure 5.13 The half resolution image of Figure 5.12	75

LIST OF TABLES

<u>Table</u>	<u>Page</u>
Table 2.1 Wildlife species of interest [5,13–20].	9
Table 3.1 The specifications for the Mesalands visit triggering computer.	15
Table 3.2 The specifications for the triggering computer for the NREL 2 visit.	16
Table 3.3 The specifications for the triggering computer for the NREL 3 visit.	17
Table 3.4 The selected IP addresses of the devices.	19
Table 3.5 The devices' selected frequencies.	20
Table 3.6 Currera-R specifications and settings.	20
Table 3.7 The specifications for the wireless contact microphone.	22
Table 3.8 The NI USB-4431 DAQ's specifications used for the analog to digital conversion of the wireless contact microphone.	23
Table 3.9 The specifications for the wireless accelerometer.	24
Table 3.10 The specifications for the audio microphone.	25
Table 3.11 The specifications for the ultrasonic microphone.	26
Table 3.12 The analog to digital converter specifications for bioacoustic microphones.	26
Table 3.13 The specifications for the visual and infrared cameras used for the optical node.	27
Table 4.1 Sensor Naming and Pairing chart	38
Table 4.2 Table of Image capture speed rate.	46
Table 4.3 The correlation between camera settings and observing taxonomic information. P=Positive, N=Negative, No=No correlation.	50
Table 4.4 An example hit of the six sensors' impact signal strength. Blade C was hit.	55
Table 5.1 The number of sensors that visually detected each impact broken down by sensor type.	71
Table 5.2 The Currera R linked max frame rate for a given resolution.	75

DEDICATION

Soli Deo Gloria.

1. Introduction

Wind energy is playing an ever increasing role in the United States' power portfolio, with a capacity of more than 62 GW. This growth will continue as another 14 GW worth of sites are under construction [1]. Offshore sites have the potential to be a part of this growth, but environmental concerns have inhibited site development. A significant concern for offshore wind turbine technology is the monitoring of bird and bat mortality through collision with blades or structures. However, impact mortality offshore cannot be assessed through the standard carcass surveys used on land. Therefore, a compact, integrated system capable of observing injury and mortality events is required to validate site-specific risk models and to demonstrate wildlife permitting compliance for offshore wind turbine sites.

As development of an integrated environmental monitoring system for offshore wind is in progress, important questions need to be answered through a rigorous research process.

What types of devices will be required for the system to monitor a wind turbine for bird and bat impacts?

How can an impact detection system be designed to be effective with the variety of sizes of bird and bat species in the Pacific Northwest?

Which sensor consistently detects collisions through a blade better, accelerometers or contact microphones?

How can camera spatial coverage of the blades be effectively maximized while maintaining high resolution for the ability to perform species identification?

Five essential sensor types have been selected to study an integrated sensor package. They are: 1) wireless accelerometers, 2) wireless contact microphones, 3) visual cameras, 4) infrared (IR) cameras and 5) bioacoustic microphones.

The system is composed of multiple nodes for each sensor type. Each sensor node will collect and send data to a central controller where the acquired data is processed and archived.

Continuous event detection is achieved using vibration sensors (accelerometers and contact microphones). The challenges associated with the sensors are filtering strike events from routine vibrations and other operational noise as well as ensuring wireless connectivity with the controller and real-time image processing for triggering cameras. Wireless connectivity and on-board battery power allow these sensors to be installed on existing turbines with minimal modifications and with a small footprint.

The optical systems, consisting of visual and IR cameras, provide the necessary information for taxonomic classification, as well as event confirmation, near misses and false positives. The technical challenges associated with the optical systems are data bandwidth and storage, and the limits in spatial coverage imposed by the field of view and cost of each instrument.

The bioacoustic microphones will provide continuous monitoring for the presence of bird songs and bat echolocation. The recordings can be used for taxonomic classification.

An event is defined as a wildlife collision or interaction with wind turbine that is detected by any sensor and confirmed by cameras.

Two system field tests were carried out and they will be referred in this document as Mesalands and NREL 2.

A literature review is presented in Chapter 2 explaining the background and motivation needed for developing of an integrated detection system for wildlife-wind turbine interactions. Chapter 3 will show the purpose, features, and settings of the vibrational sensors, cameras, and bioacoustic microphones selected to be incorporated into the system. It will then elaborate on the system's network design, software architecture, and integrated components. Individual component placement locations and performance for the two field tests will be presented as well.

The experimental testing procedures and the theoretical methods will be documented in Chapter 4. The experimental testing procedures will explain the steps followed to perform the laboratory testing, field testing, and image collection for the evaluation of camera settings. Topics within the theoretical methods will include the techniques applied for examining the field test data and the images used for determining the camera settings, as well as the design and evaluation of the potential automatic detection algorithm. Chapter 5 will present the experimental results for the sensors and the

complete system, explaining the implications of the results in reference to future system deployment. Finally, conclusions and suggestions for future work will be discussed in Chapter 6.

2. Background and Literature Review

In this chapter, the main subjects related to this project are presented, starting with the background and literature review of environmental monitoring techniques for wind turbines and the barriers for offshore wind turbine site development. A brief review of current studies and systems used to monitor volant animal interaction with wind turbines is then explored. An explanation will be given for the five selected bird and bat species used as small sample size to optimize developed system. Finally, a list of signal processing and camera image collection terminology will be explained.

As part of the renewable power generation, wind power will play an increasingly important role in the coming decade. The expected total capacity will double today's numbers by the end of 2018, going from 300 GW to nearly 600 GW [1]. In United States, there are now more than 46,300 operating utility-scale wind turbines according to American Wind Energy Association (AWEA) [2], and 20% of the electricity generation is expected to come from wind resources by 2030 [3]. Therefore, it is imperative to understand the environmental impact of these devices as they became more abundant, especially for those wind sites that are threatening endangered species.

As offshore wind grows, "it is imperative that this development not impact avian and bat species, particularly those that are threatened or endangered. This risk can be mitigated through environmental impact assessments prior to installation and monitoring programs once projects are in operation. While onshore wind energy projects are subject to similar scrutiny, established methodologies for assessing mortality of avian species through carcass collection [4] are infeasible in the offshore environment. Consequently,

for offshore wind to realize its renewable generation potential without impacting volant species, new and economical approaches to environmental monitoring are required.” [5]

2.1.Environmental Monitoring Techniques for Wind Turbines

Statistics of wildlife interaction with land-based wind turbines are generated through ground-based carcass studies conducted around a wind farm by trained biologists.

While carcass surveys are the standard protocol for quantifying mortality at onshore sites, this method is imperfect due to infrequent surveys at remote sites, removal of carcasses by scavengers between surveys, and delays of days to weeks in obtaining information on collision events. Furthermore, carcass surveys are not feasible at offshore wind energy sites, and there is currently no practical analogue for collecting these statistics in a marine environment.

Therefore, new, economical and appropriate monitoring methods need to be developed, particularly for offshore conditions. One potential approach has been carried out is by setting up either visual or infrared camera systems [5].

2.2.Bird and Bat Monitoring Techniques

2.2.1. Thermal Animal Detection System

One approach used for avian and bat interaction studies with wind turbines is the employing of a camera system. Both visual- or infrared-spectrum cameras have been used in monitoring studies. While visual camera imagery is more effective for species identification because of high pixel resolution and color contrast, infrared (IR) systems are able to operate over a broader range of environmental conditions (e.g., operation at night).

One notable IR system is Desholm et al.'s [6] Thermal Animal Detection System (TADS), which achieved taxonomic classification through wing beat analysis and animal size, in addition to detection. Detection and identification functions were not automated and required manual review of imagery collected [6].

2.2.2. WT-Bird

“One approach for automatic detection of avian and bat collision with wind turbines is vibrational or acoustic sensing devices. Wiggelinkhuizen et al. [7] developed the WT-Bird bird collision monitoring system. The system initially only employed wired contact microphones for the blades before finally selecting wired accelerometers to improve durability and signal-to-noise ratio [7]. This work indicated that it should be feasible to detect strike events from the resulting structural vibration.”[5] Once a collision event is detected, the visual cameras are triggered so that only imagery of greatest interest was saved.

The WT-Bird system was the first unit to use sensors to trigger visual cameras for a concise event recording for later viewing to perform species identification. The system uses two visual cameras placed on the tower looking up, orientated 180° apart from each other. The cameras were mounted on tripods looking up with a one meter offset from the tower wall and a nine meter offset from the ground. The field of view for this camera placement was approximately 90% of the rotor sweep [7].

Generation of artificial impact events using dummy birds was required for field testing. Many ideas were proposed (e.g., using a tennis ball server placed on top of the

nacelle) and a few were developed (e.g., static rigging attached to side of the wind turbine with a collapsible arm that the turbine yawed into and collapse the arm). Developers of the WT-Bird system found sand bags [8] and weighted tennis balls launched with a “gas-pressurized launcher” effective at generating impact events [7].

2.2.3. DTBird

DTBird is a real-time optical detection system, capable of identifying avian near-wind turbine interactions. The system uses machine vision object tracking software to monitor the wind turbine’s surroundings. Detection is made with four high definition cameras; they provide a 360° view of blades and nacelle from their fixed positions located on the tower [9]. A DTBird subsystem, DTBat, uses ultrasound recognition to detect bat presents. The data is recorded as a sonogram [10].

2.3. Wireless Accelerometer Evaluation Studies

In exploring similar applications of vibrational sensors used mounted to a wind turbine, two studies were identified for their use of wireless accelerometers in the application of structural health monitoring [11][12]. Swartz et al. mounted wireless accelerometers at four different heights inside the tower. Carbajo et al. compared three different wireless accelerometers for the application of blade damage detection. The sensors were mounted to a wind turbine blade.

2.4. Species of Interest

Special design consideration was given to Pacific Ocean marine birds and coastal bats of the Northwest. Taxonomic information from a small sample size of five mostly

protected bird and bat species were used to optimize camera placement and settings. The bird species selected were cassin's auklet (*Ptychoramphus aleuticus*) for small-sized species, western gull (*Larus occidentalis*) for medium-sized species, and short-tailed albatross (*Phoebastria albatrus*) for large-sized species. The hoary bat (*Lasiurus cinereus*) and silver-haired bat (*Lasionycteris noctivagans*) were two bat species selected because they have been sited offshore. These bats are comparable in size to the smallest marine birds, but considerably smaller than most marine birds. Table 2.1 compares the range of body lengths, wingspans and masses that the five selected volant animals cover [5].

Table 2.1 Wildlife species of interest [5,13–20].

Species Representative Size	Small Bird	Medium Bird	Large Bird	Small Bat	Small Bat
Species	Cassin's auklet	Western gull	Short-tailed albatross	Hoary bat	Silver-haired bat
Body length	22.9 cm	61.5 cm	91.4 cm	13.0 - 15.0 cm	9.4 - 11.4 cm
Wingspan	38.1 cm	137.2 cm	220.98 cm	37.1 - 41.7 cm	26.9 – 30.7 cm
Mass	200 g	1100 g	6400 g	26.0 g	10.0 g

Figure 2.1 and Figure 2.2 show for size comparison a marbled murrelet (*Brachyramphus marmoratus*), cassin's auklet, western gull, and laysan albatross. The marbled murrelet (24 cm body length, 40.6 cm wingspan, 202 g mass) is included in Figure 2.1, Figure 2.2 and Figure 2.4 for comparison because like the cassin's auklet they are similar in size and a protected species. The layson albatross (*Phoebastria immutabilis*) was used in the comparison images because of availability at the OSU Department of Fisheries and Wildlife's Birds and Mammals Collections. The layson albatross is a smaller (199.4 cm wingspan) and a more commonly sighted bird on the Pacific Northwest coast than the short-tail albatross. Figure 2.5 compares the hoary bat and the silver-haired bat [21].



Figure 2.1 Marbled murrelet (top), cassin's auklet (second from top), western gull (third from top), and laysan albatross (bottom).



Figure 2.2 Marbled murrelet (top), cassin's auklet (second from top), western gull (third from top), and laysan albatross (bottom).



Figure 2.3 Western gull (top), and Laysan albatross (bottom).



Figure 2.4 Marbled murrelet (top), Cassin's auklet (bottom).



Figure 2.5 Silver-haired bat (top) and hoary bat (bottom).

“The siting of terrestrial wind facilities has greatly influenced the extent of bird and bat impact mortality, and similar concerns exist in the placement of offshore renewable energy facilities. Areas of high animal density, low density, and migration corridors occur over certain areas, often associated with key marine habitat features such as water depth, shoreline topography, and distance to shore [22]. For example, along the U.S. west coast, the inner continental shelf bird community is dominated by heavy bodied diving species with relatively low flight heights (often < 10 m), whereas the outer shelf-slope and offshore communities are dominated by surface feeding and dynamic soaring species with greater flight heights (10s–100s m) [22,23]. Such flight behavior greatly influences potential” wind turbine collision locations [5].

2.5. Wavelet Analysis

“Wavelet analysis is a powerful tool for joint analysis of time and frequency domains. Applications include operation and maintenance, media and image file compression, and engine knock detection [24–26]. In our case, wavelet analysis is implemented to distinguish collision events from routine vibration. Wavelet analysis decomposes the signal of interest into sinusoids. Convolution is then performed by comparing a “mother” wavelet with the decomposed signal. A mother wavelet is a wave shaped oscillation that begins and ends at zero amplitude. A preliminary search has been performed to find a suitable mother wavelet for this application.... A Coiflets 5 mother wavelet (impulsive signal) is being used. Using this mother wavelet, multiple convolution passes are performed on the signal. The results are improved by adjusting the scaling function and the mother wavelet during each analysis pass. A significant benefit to wavelet analysis is that it can be performed in real time [25,27]”[5].

2.6. Ring Buffer

All sensors will utilize circular (or ring) buffers for the purpose of short-term data collection to reduce data storage requirements associated with archiving continuous streams from high-bandwidth sensors, such as visual-spectrum cameras. A ring buffer can be structured to archive data from both sides of an event (e.g., collision). This architecture will reduce the volume of data needing to be manually evaluated and allow for constant and unattended data collection [5]. Figure 2.6 give a visual walkthrough of a ring buffer.

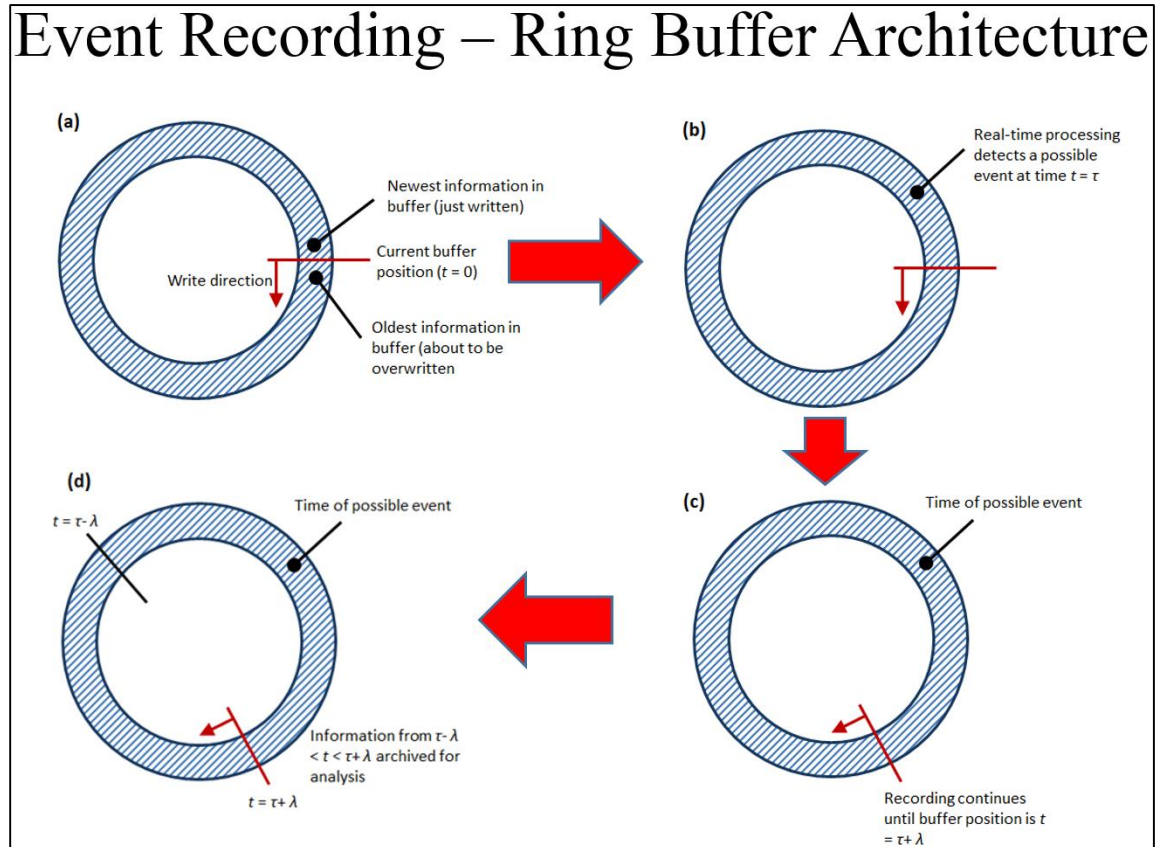


Figure 2.6 Ring buffer architecture and event detection. (a) normal operation. (b) event detection trigger. (c) buffer continues to write to capture information on both sides of the event. (d) contents of buffer archived for subsequent analysis [28].

3. Component Selection and System Design

This chapter explains how the sub-systems, 1) vibrational sensors and smart cameras, 2) the bioacoustic microphones, and 3) the optical camera node (Infrared and visual cameras), were integrated to compose the final system. First, the individual components will be discussed to explain their key features, how they are configured and operated, and then, the system setup of the components will be explained for two field tests.

3.1.Component Selection

3.1.1. Triggering Computer and Labview Programming

For the first system field test at Mesalands, the software programs used to operate the contact microphones and the smart cameras consisted of Labview programs, and the accelerometers were controlled using the manufacturer's proprietary software. The Mesalands triggering computer specifications are given in Table 3.1.

Table 3.1 The specifications for the Mesalands visit triggering computer.

Triggering Computer	Mesalands Visit
Processor	Intel Xeon, Quad-Core, 2.4 GHz
RAM	8 GB
Hard drive	300 GB
Gigabit Ethernet ports	1
USB 2.0 ports	4
Operating system	Windows 7
Additional programs	Labview 2012

The integrated system uses a central computer to trigger the saving of the components' ring buffers; the data from the all of the ring buffers can be saved with a single system trigger to the triggering computer.

When the integrated system was tested at the NREL 2 visit, the research team used a high quality laptop for the triggering computer. The triggering computer specifications are shown in Table 3.2. Because of the limited USB and Gigabit Ethernet ports installed on the laptop, it was challenging to developing a plan for the NREL 2 visit where all of the cameras and receivers could be connected to the computer while still maintain full functionality.

Table 3.2 The specifications for the triggering computer for the NREL 2 visit.

Triggering Computer	NREL 2 Visit
Processor	Intel i7 4th, Quad-Core, 2.4 GHz
RAM	16 GB
Solid state drive for operating system	256 GB
Hard disk drive	2 x 1 TB
Gigabit Ethernet ports	1
USB 2.0 (3.0) ports	1 & (3)
Operating system	Windows 7
Additional programs	Labview 2013

After the NREL 2 visit, it was decided that a custom computer would be built and used for the upcoming NREL 3 visit with sufficient number of USB and Gigabit Ethernet ports, fast enough processor, and large enough memory and hard drive space. The specifications for the NREL 3 computer are shown in Table 3.3.

Table 3.3 The specifications for the triggering computer for the NREL 3 visit.

Triggering Computer	NREL 3 Visit
Processor	Intel Xeon, Quad-Core, 2.4 GHz
RAM	32 GB
Solid state drive for operating system	500 GB
Hard disk drive	2 x 1 TB
Gigabit Ethernet ports	4
USB 2.0 (3.0) ports	8 & (4)
Operating system	Windows 7
Additional programs	Labview 2012

The programs used to operate, adjust, and record the system's components were written in Labview. Network variables and ring buffers were key Labview features utilized for the programming in this project. Network variables were used in Labview for communicating between three .vi files running on the computer, software triggering smart cameras, and receiving data from devices; Figure 3.1 shows this interaction. For this interaction, the operator manually triggers the system (#1 in the figure) in the Vibrational Sensor .vi. Then, a network variable is changed to initiate the Triggering .vi (#2). The devices' programs are prompted by the Triggering .vi to save (#3). Each device's ring buffer is saved to the triggering computer (#4).

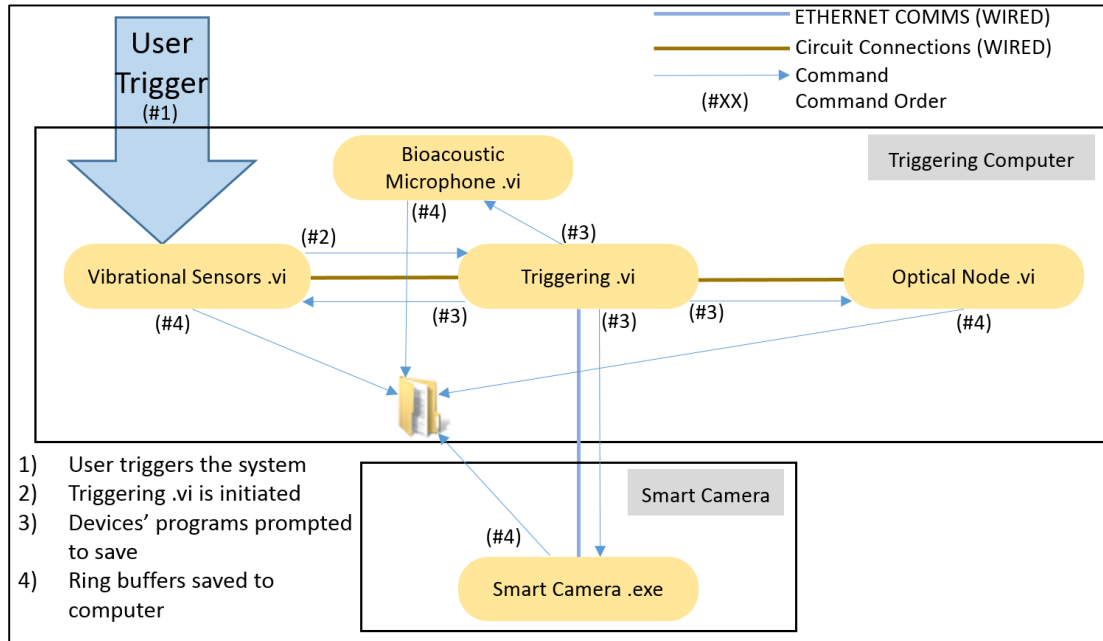


Figure 3.1 A diagram of the communication between Labview programs.

For the NREL 2 visit, the system was triggered manually. Automated triggering algorithms are currently being developed to trigger the system using machine vision for IR cameras in the optical node and analysis for the vibrational sensors.

3.1.2. Local Network Design

A local Wi-Fi network was designed to remotely communicate with the computer located in the nacelle. A long range high-powered wireless outdoor access point was used to create the local network for the system testing. Using remote desktop and a second laptop on the ground, the team was able to adjust settings and trigger the system on the computer while the wind turbine was in operation.

The IP addresses of the networked communication between computers, cameras, and the wireless access point was planned prior to installation, see

Table 3.4. A fixed subnet mask and fixed IPs were used to setup the local network. A separate network was used for interacting with the optical node because the infrared cameras have permanent factory set IP addresses and all the cameras in the node share an Ethernet switch. The 255.255.0.0 subnet mask was used for all of the non-roaming IP addresses. A diagram of the system's local network is shown in Figure 3.2 used in the testing of system for communicating between operators during set up and testing.

Table 3.4 The selected IP addresses of the devices.

Device / Network Card	IP Address
Currera-R #1	10.0.0.2
Currera-R #2	10.0.0.3
Flur #1	169.254.2.4
Flur #2	169.254.40.36
Manta BW	169.254.0.1
Manta Color	169.254.1.2
Ground computer wireless card	10.0.0.20 or roaming
Ground computer Ethernet port	10.0.0.1
Triggering computer wireless card	Roaming
Triggering computer usb wireless card	10.0.0.7

Table 3.5 shows the wireless communication devices used in the system, the select frequency, and whether device has an adjustable frequency. The system's frequencies also had to be adjusted for the testing site's wireless communications such as Wi-Fi.

Table 3.5 The devices' selected frequencies.

Device Frequency	Selected Frequency	Adjustable Frequency
Microphone A	UHF-A	No
Microphone B	UHF-B	No
Microphone C	UHF-C	No
Accelerometer A	2.470 GHz	Yes
Accelerometer B	2.475 GHz	Yes
Accelerometer C	2.480 GHz	Yes
Wireless access point	2.432 GHz	Yes
Two way radios	462.7250 MHz	Yes

3.1.3. Smart Camera

The visual camera selected, tested, and system integrated was the Currera-R Camera. A smart camera is a scientific camera with an embedded CPU and operating system. Visual cameras allow the operator of the system to perform species identification using visual taxonomic information. The specifications for the smart camera are listed in Table 3.6.

Table 3.6 Currera-R specifications and settings.

Camera Type	Visual Smart Camera
Manufacturer	Ximea
Model	Currera-R RL50C-OC
Frame rates	15, 45, 80 fps
Sensor resolution	2592 x 1944
Pixel depth	24 bit RGB, 8 bit Mono, 16 bit Mono, 8 bit RAW, 16 bit RAW
Field of View	Wide 25.7° x 19.4°, Tele 4.35° x 3.27°
Focal Length	12.5 - 75 mm
Processor	1.6 GHz
RAM	1024 MB
Hard drive	3.6 GB SSD
Operating system	Window XP Embedded

For testing purposes a variable focal length lens was selected for the project. Using a zoom lens allowed for multiple camera placement locations to be tested thoroughly. The widest field of view setting for the lens is $25.7^\circ \times 19.4^\circ$, and the telescopic field of view setting is $4.35^\circ \times 3.27^\circ$.

The Currera-R was selected to reduce data bandwidth sent to the triggering computer and for future applications of its onboard processor. Using the Currera-R's embedded CPU and operating system allowed for a Labview executable file to run the camera. Images taken by the camera would be stored on the camera's RAM in a ring buffer and only sent to the computer if triggered. In a conventional camera, all images would be sent to the computer to be stored and processed on the computer's RAM. Because the smart camera's ring buffer is limited to the camera's RAM size, the file size of the desired number of images captured has to be determined in advance so not to exceed the RAM. Additional image processing could be performed on the camera's CPU such as using machine vision to process individual frames for birds or bats.

The exposure, the frame rate, the total number of captured images and the location of trigger point within the buffer are all settings with in the camera program that can be selected by the user. Resolution, max frame rate and bit depth determines effects the required processing power needed for image acquisition. A resolution of 1296×972 with a max frame rate of 45 fps, and an 8 bit mono image setting for the bit depth. A 15 image ring buffer (.825 second window at 18.18 Hz sampling) and a .05 sec exposure time were used for the NREL 2 testing.

3.1.4. Vibrational Sensors

Two vibrational sensors were evaluated for the system: a contact microphone and an accelerometer. The contact microphones were used to collect structure borne noise traveling through the blades, and the accelerometers collected the accelerations. Both vibrational sensors are used to monitor the blades of the wind turbine for animal collisions. The system would be triggered to save the data once an event (i.e., bird/bat collision) was detected. A contact microphone and an accelerometer were mounted to each blade.

The microphone selected was the analog wireless contact microphone-receiver pair, USK-40 (sensor) and UZ-10 (receiver); specifications are given in Table 3.7. An analog wireless contact microphone was selected because of a lack of digital scientific grade contact microphones available on the market. The microphone's signal is digitized using a USB-4431 DAQ. The USB-4431 DAQ specifications are listed in Table 3.8.

Table 3.7 The specifications for the wireless contact microphone.

Device Type	Wireless Contact Microphone
Manufacturer	Sun-Mechatronics
Model	USK-40 (sensor), UZ-10 (receiver)
Sampling rate	Continuous (Analog)
Transmission frequency	Ultra high frequency-A,B,C
Transmission range (line of site)	80 - 150 m

Table 3.8 The NI USB-4431 DAQ's specifications used for the analog to digital conversion of the wireless contact microphone.

Device Type	Analog to Digital Converter
Manufacturer	National Instruments
Model	USB-4431 DAQ
Sampling rate	up to 102.4 kHz
Analog to digital resolution	24 bit
Voltage input range	± 10 V
Channels	4 input, 1 output

The USB-4431 DAQ was selected for the analog to digital conversion of the microphone's signal because of its 24 bit resolution and its scientific grade equipment quality. Even though the microphone's signal output only has max peak to peak signal of $\approx \pm 15$ mV, the DAQ offered the highest steps/mV among National Instruments products at 838.8 steps/mV. The DAQ's 102.4 kHz max sampling rate was more than sufficient for the project's needs.

The accelerometer selected was the digital wireless accelerometer-receiver pair, G-Link LXRS (sensor) and WSDA-Base 104 (receiver). Prior to transmission, the sensor's signal is digitized within the sensor.

The G-Link LXRS digital accelerometer was chosen for its sufficient range (up to 2 km), Labview compatibility, triaxial capabilities, and sampling rate (max 512 Hz); its lossless packet communication protocol was able to retransmit lost or damaged data packets. If a sensor's data packet is not received or only partially received by the base station, the base station will ask the sensor to retransmit the packet. The lossless packet communication protocol significantly reduces loss of sensor's data due to loss of line of sight and interference (microstrain.com). Unlike the accelerometer, the analog microphone

was susceptible to loss or distortion of data due to line of sight loss and interference. More wireless accelerometer's specifications are shown in Table 3.9.

Table 3.9 The specifications for the wireless accelerometer.

Device Type	Wireless Accelerometer
Manufacturer	Lord-MicroStrain
Model	G-Link LXRS (sensor), WSDA-Base 104 (receiver)
Sampling rate	512 Hz
Transmission frequency	2.405 to 2.480 GHz
Transmission range (line of site)	2 Km
Measured Axes	3
Accelerometer range	± 10 G
Analog to digital resolution	12 bits at transmitter

The selected microphone sampling rate was 1000 Hz resulting in a cutoff of 500 Hz as the recording's highest observable frequency (Nyquist frequency). With this sampling rate any impact could be observed over the repeating frequencies of operational background noise (i.e. generator, generator shaft, and blade rotation). The selected sampling rate for recording the accelerometer's signal was 512 Hz, the device's max sampling rate. The resulting Nyquist frequency for this sampling rate is 256 Hz, which would still give clearance from operational noise.

For the design of the vibrational sensor software, the sampling rate, length of the triggered event recording, and the triggering point within the buffer are user selected. After testing the initial program at the NREL 2 visit with the triggering point within the buffer being fixed to the end of the recording, it was decided that for testing purposes the trigger point should be user selected. For the vibrational sensors, a five second recording was selected as the buffer size for the NREL 2 system testing.

3.1.5. Bioacoustic Microphones

The bioacoustic subsystem uses two types of microphones, an audio and an ultrasonic microphone. A G.R.A.S. piezoelectric, free-field microphone was selected for the audio microphone; this microphone will be used to record bird songs and other audible wildlife calls, with a microphone frequency range of 10 – 20,000 Hz (www.gras.dk). The microphone's sampling rate will be set to 20 kHz. An UltraSoundGate electret, ultrasonic microphone was selected to detect bat echolocation and other ultrasounds. The microphone has a frequency range of 10 – 120 kHz (www.avisoft.com); its selected sampling rate will be 50 kHz. Both microphones will save a 10 second ring buffer and will be powered using two external power supplies for delivering the excitation voltage. The signals will be acquired digitally using the NI-9223 module and the NI cDAQ 9171 USB chassis combination. The specifications for the audio microphone (Table 3.10), the ultrasonic microphone (Table 3.11) and the analog to digital converter (Table 3.12) are listed in the tables below.

Table 3.10 The specifications for the audio microphone

Device Type	Audio Microphone
Manufacturer	G.R.A.S.
Model	40PH
Sampling rate	Continuous (Analog)
Frequency range	10 - 20k Hz
Power supply	2 - 20 mA

Table 3.11 The specifications for the ultrasonic microphone.

Device Type	Ultrasonic Microphone
Manufacturer	UltraSoundGate
Model	Knowles FG (# 40001)
Sampling rate	Continuous (Analog)
Frequency range	10 - 120 kHz
Power supply	5 V, 14 mA

Table 3.12 The analog to digital converter specifications for bioacoustic microphones.

Device Type	Analog to Digital Converter
Manufacturer	National Instruments
Model	# 9223
Sampling rate	up to 1 MHz
Analog to digital resolution	16 bit
Voltage input range	± 10 V
Channels	4 input

3.1.6. Optical Camera Node

The benefits of stereo vision for species identification were explored using two visual Manta G-210 cameras and two infrared A655sc cameras. The effectiveness of color verses grayscale images for species identification were compared using one color and one grayscale Manta G-210 camera. The cameras' specifications and settings are listed in Table 3.13.

Table 3.13 The specifications for the visual and infrared cameras used for the optical node.

Camera type	Infrared	Visual color	Visual grayscale
Manufacturer	FLIR	Allied Vision	Allied Vision
Model	A655sc	Manta G-210C	Manta G-210B
Max frame rate	50 fps	14 fps	14 fps
Sensor resolution	640 x 480	1624 x 1234	1624 x 1234
Pixel depth	12 bit	32 bit RGB	12 bit Mono
Max data bandwidth	≈ 0.25 Gb/s	≈ 1 Gb/s	≈ 0.35 Gb/s
Field of View	15° x 11.3°	52° x 445°	52° x 445°
Focal Length	44 mm	Hyper focal	Hyper focal
Wavelength	7.5 - 14.0 μm		
Detector Pitch	17 μm		
Temp Range	-20°C to 150°C		
Temp Accuracy	±2°C or ±2%		
NETD	<50 mK		

“Particularly for IR cameras, image resolution may be insufficient for taxonomic classification of targets. One approach to provide additional information is the use of camera pairs at a fixed baseline separation and orientation to produce stereo imagery. A calibrated stereo camera can be used to determine the size and three-dimensional location of targets in space. This is a powerful capability for distinguishing collisions from near misses, as well as providing information about body length and flight speed for taxonomic classification. This capability is being developed for both the infrared and visual spectrum cameras in the instrumentation package” [5].

For the design of the camera program, the exposure, the frame rate, number of images captured and the trigger point within the ring buffer is user selected. The highest resolution, max frame rate, and best bit depth was chosen for both types of cameras. The images from the cameras will be sent to the main computer to be processed and stored in the buffer. A 60 image ring buffer (10 second window at 6 Hz sampling) was chosen for

the visual cameras, and for the IR cameras, a 120 images (10 second window at 12 Hz sampling) was chosen for the ring buffer size.

3.1.7. Compressed Air Cannon

After examining the feasibility of the ideas, risk of damaging the wind turbine blades, the flexibility of locating the collision on the blades, and the flexibility of variety of projectiles able to be launched, a compressed-air cannon was constructed to create impacts for testing. The compressed-air cannon uses either an air compressor or a pre-pressurized air tank as its propellant source. The regulator for the air cannon is set to 115 psi (the limit pressure for the electric valve). The launcher is controlled using an off/on toggle safety switch and a momentary switch. The air cannon's charging tank is charged and operated by holding down and then releasing momentary switch to open the valve and launch the tennis ball. The switches control the electric pneumatic valve using a 24 VDC battery.

3.2. System Design

3.2.1. Mesalands Visit System Design

The system's first field test was performed at the North American Wind Research and Training Center (NAWRTC) at Mesalands Community College in Tucumcari, New Mexico. This testing occurred December 9th to December 13th of 2013. The primary purpose of the Mesalands testing was to gather recordings from the vibrational sensors. The collected recordings included simulated blade impacts as well as recordings of the wind turbine while under normal operations (start up, shut down, generator engagement,

pitching/yawing actions etc.). A sequences of camera images were also collected from the smart cameras.

The vibrational sensors were mounted at the root of blades with the receivers and the main computer located on the ground. The sensor placement was chosen to maintain the aerodynamic efficiency of the blades. The location also allowed for easy installation and maintenance of the sensors. Images from the smart camera were taken from both the top of the nacelle and the base of the tower. Figure 3.2 shows a wiring diagram of the equipment setup at Mesalands. Figure 3.3 shows a diagram of the equipment placement on the wind turbine for the Mesalands testing. The air cannon shown in the figure was used to generate the simulated impacts.

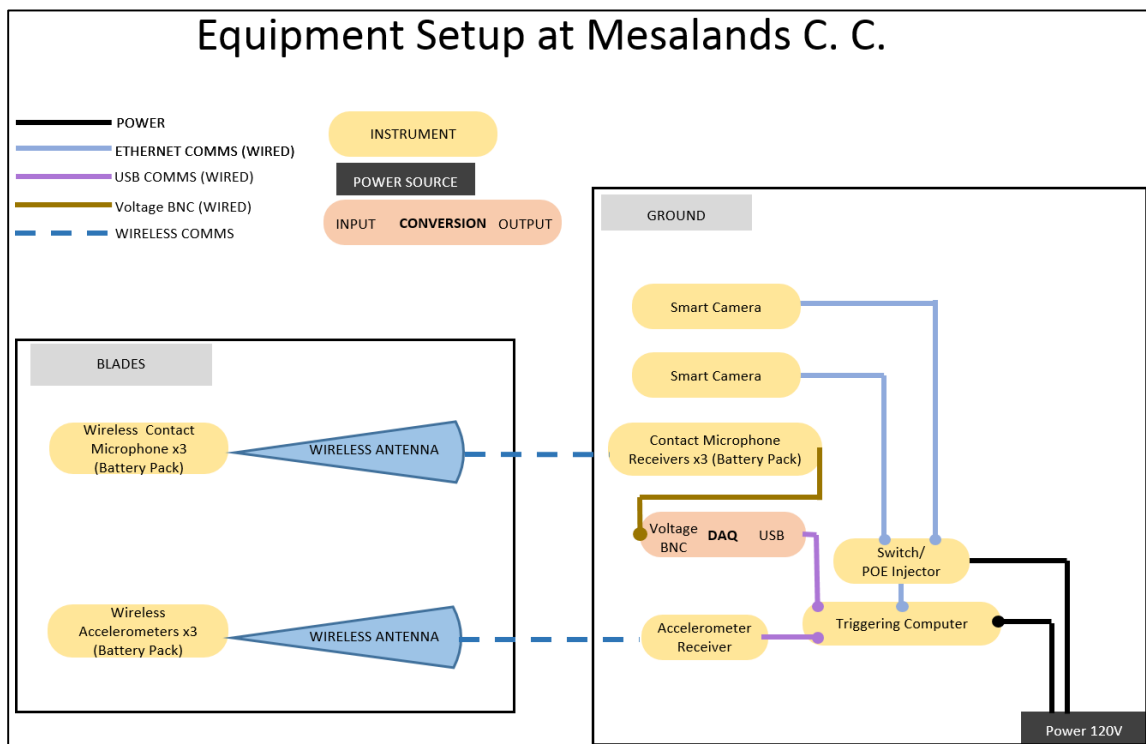


Figure 3.2 Wiring diagram of the equipment placement at the Mesalands visit.

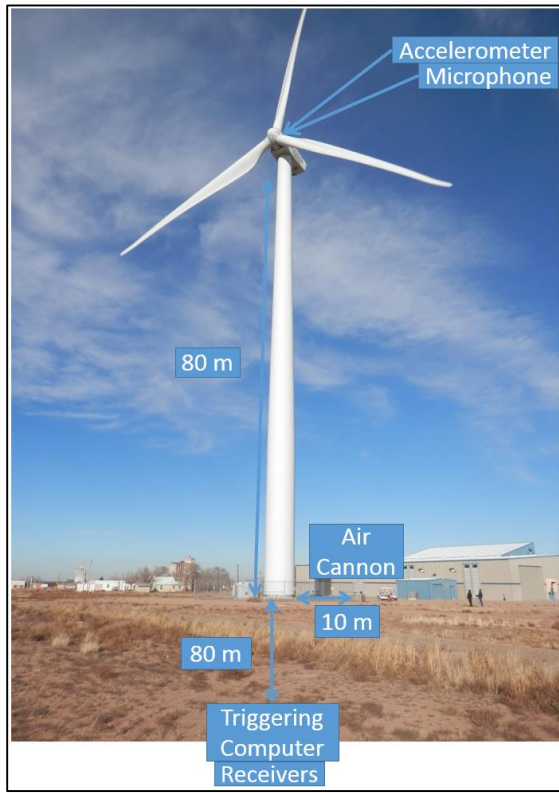


Figure 3.3 Diagram showing the equipment placement on the wind turbine for the Mesalands testing.

3.2.2. NREL 2 Visit System Design

The system's second field test was performed at the National Wind Technology Center at National Renewable Energy Lab in Boulder, Colorado. This testing occurred October 20th to October 24th of 2014. The NREL 2 visit was the first complete system field test. The purpose of the test was to evaluate the quality of the system integration, and to collect data from all devices with a single trigger. Images and recordings were taken during simulated impacts as well as normal operational conditions.

For the system tests the main computer was placed inside the nacelle for close proximity to the cameras and the receivers. Using remote desktop, a second computer on the ground was used to trigger the system. The wireless access point was placed on the

ground with the second computer. Like Mesalands, the same location was chosen for the vibrational sensors. The receivers were placed inside the nacelle by the main computer. The smart cameras, bioacoustic microphones, and the optical node were all placed on top of the nacelle. The smart camera on tripods were attached to the nacelle's safety cage. The bioacoustic microphones were mounted to the safety cage. This location was chosen for ease of access. Another proposed location for testing was on outside of the tower; this location was not selected because of its more complicated installation. The optical node was mounted to a pan-and-tilt frame. The frame allowed for multiple camera angles of the blades from the nacelle to be tested without manual readjustment. The pan-and-tilt frame was also mounted to the safety cage. Like for the Mesalands testing, an air cannon was used to generate the simulated impacts. Figure 3.4 shows a wiring diagram of the equipment setup at NREL 2. Figure 3.5 shows a diagram of the equipment placement on the wind turbine for the NREL 2 testing.

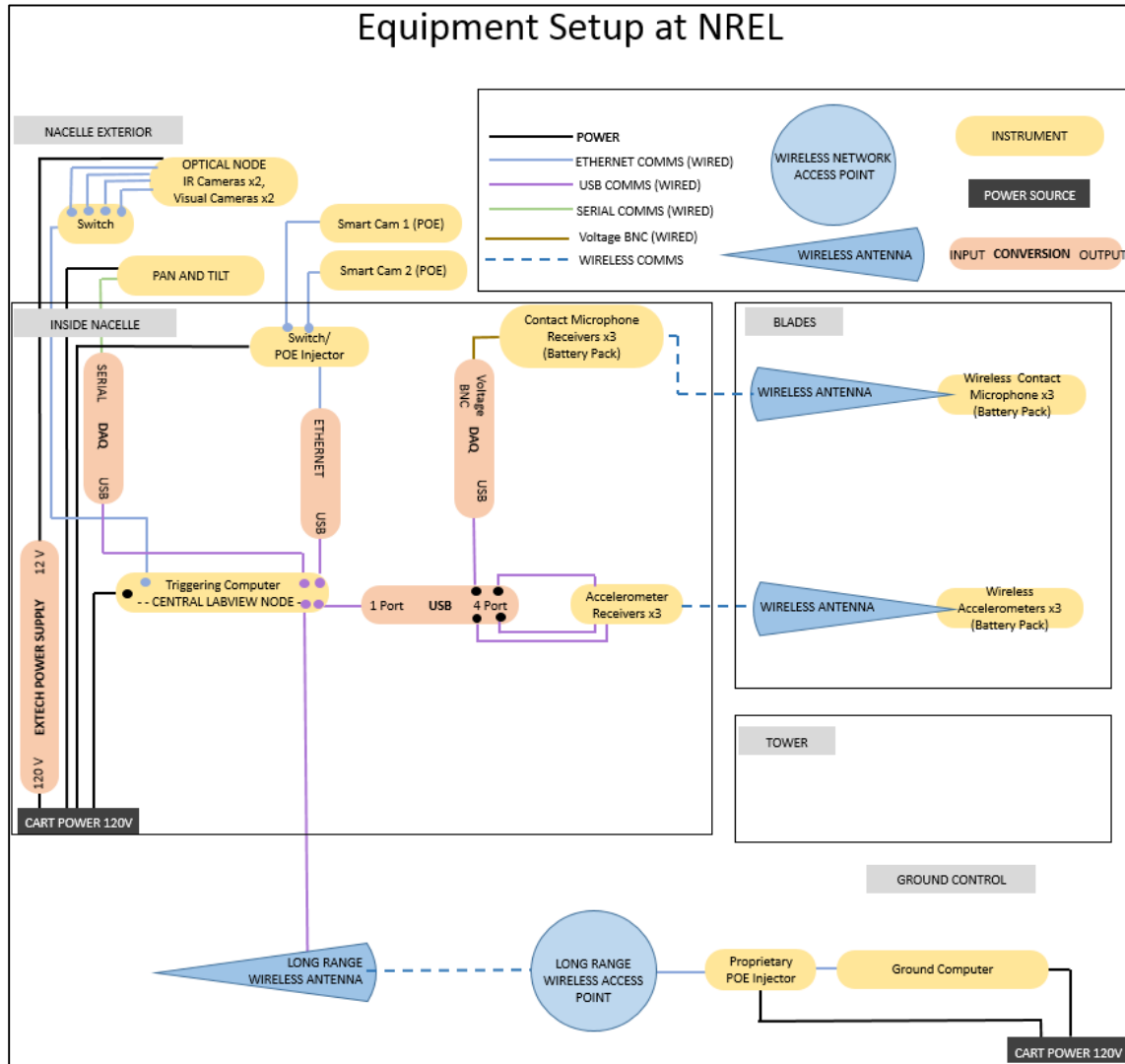


Figure 3.4 Wiring diagram of the equipment placement for the NREL 2 visit.

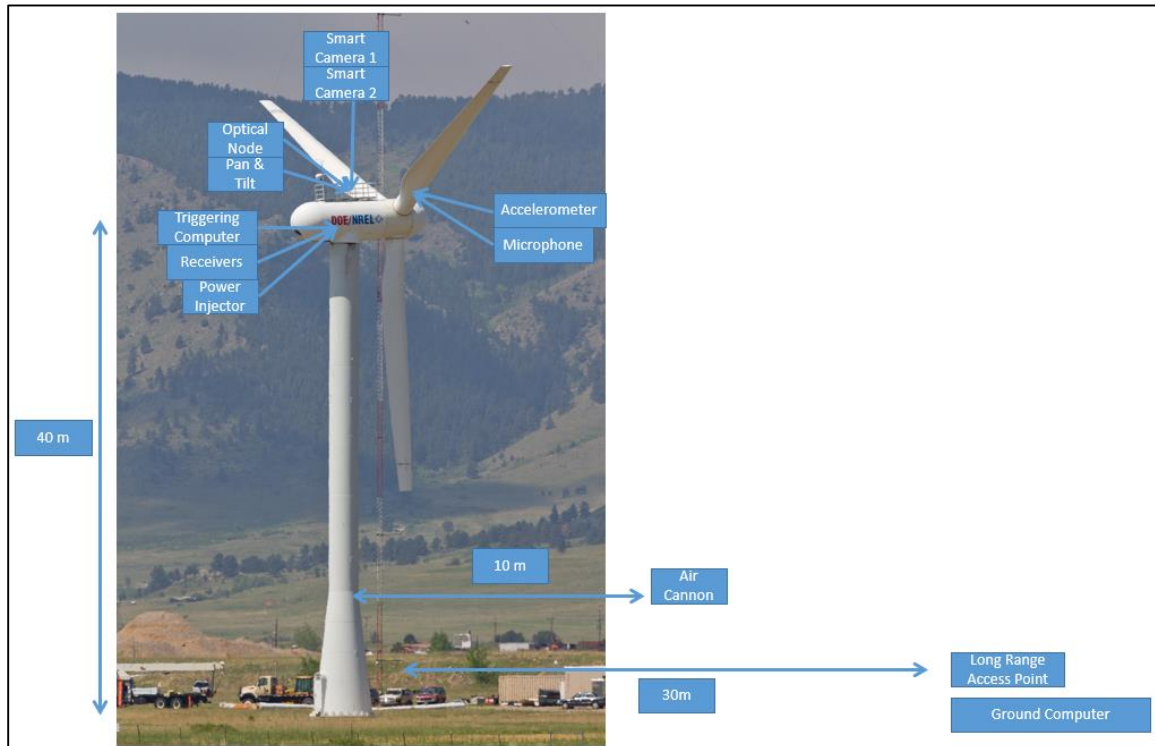


Figure 3.5 Diagram showing the equipment placement on the wind turbine for the NREL 2 visit.

4. Methodology

In this chapter, both the experimental and theoretical methodology will be discussed. The experimental methods will cover the procedures for the lab testing, Mesalands and NREI field testing, and testing of the camera settings at Newport. The theoretical methods will cover the procedures for examining the field test data, developing an image pixel simulator, and adapting the wavelet analysis as an event triggering algorithm.

4.1. Experimental Procedures

4.1.1. Lab Testing and Validation

During the early stages of the project's development, several lab tests were performed for the evaluation and verification of the system's components and data post processing. During the first stages of exploring wavelet analysis for application of event detection, a sine wave with superimposed deltas was created for simulating an event masked by operational noise. "Further laboratory evaluation involved data collection from an accelerometer and a contact microphone attached to a programmable shaker table" [5].

These laboratory simulations included a sine wave interspersed with impact events (represented using impulsive transients) to reproduce an event masked by background noise. The resulting synthetic time series was used to select the candidate mother wavelet described above [5]. [5]. Through the creation of the synthetic signals and signals collected from the sensors recording the shaker oscillations, the tuning of the system's wavelet for event detection was initiated. Key sensor tendencies were discovered through this testing.

The selected sampling rate for the testing was 512 Hz for accelerometers and 1000 Hz for microphones

Figure 4.1 Top is an example of a raw signal from a wireless accelerometer installed on the table attached to the shaker. During the recording with the shaker operating at various frequencies, impact events were simulated by tapping on the shaker platform. The shaker input function was a basic sine wave of $y = .1 * \sin(2 * 100 * \text{Pi} * t)$. The wireless accelerometer's sampling frequency was 512 Hz. The recording was then examined using wavelet analysis to assess if the algorithm amplified the tapping and reduced the noise represented by the shaker oscillations. In comparing the signal to the wavelet pass (Figure 4.1 B), the tapping was amplified using the wavelet analysis.

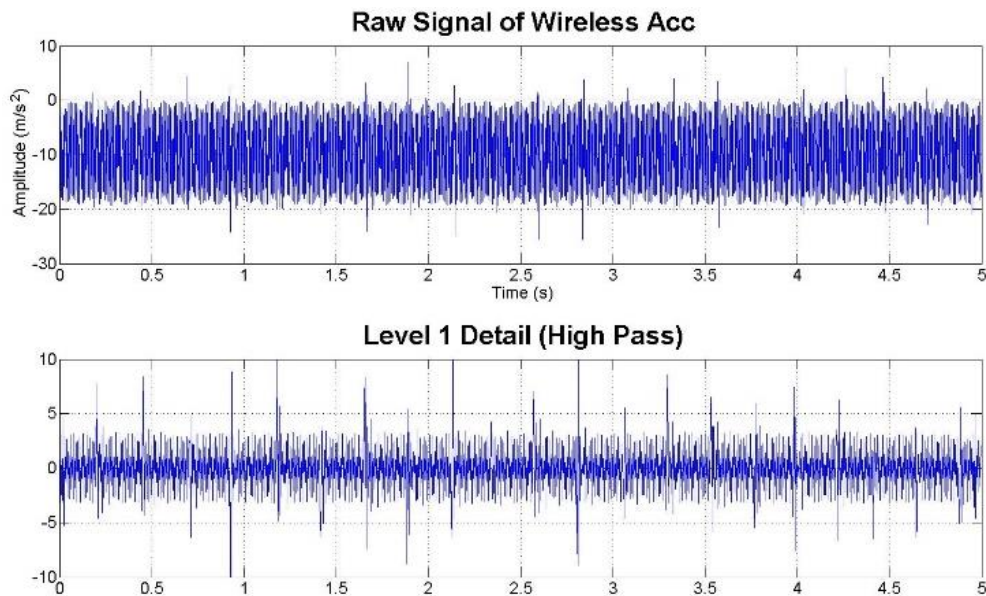


Figure 4.1 (T) raw signal from accelerometer attached to shaker (B) wavelet analysis of signal

In addition to sensor function, laboratory studies also assessed the sensors' wireless connectivity. The wireless sensors' transmission capabilities were tested by evaluating the

sensors' connectivity at the required transmission range and in an environment with interference comparable to that occurring during the field testing (e.g., Wi-Fi networks and wind turbine generator) [5].

4.1.2. Mesalands Community College Field Testing

The wind turbine used for testing at Mesalands was a GE 1.5 MW ESS. The turbine has a 37 m blade length and an 80 m hub height. Over the five day testing period, accelerometers and contact microphones were installed on each blade, images were taken with the Currera R camera from the ground and nacelle, and vibrational recordings were taken of the wind turbine during normal operations and during generation of simulated impacts using an air cannon to launch tennis balls at the blades and tower.

A detailed operational itinerary was developed in order to stay organized and achieve the required testing objectives for the trip. Another organization tool used for planning the trip was a detailed packing list.

One wireless accelerometer and one wireless contact microphone were mounted to the root of each wind turbine blade (Figure 4.2). A procedure for mounting the sensors to the blades was established with guidance and approval from the facility staff.



Figure 4.2 An image of the sensors mounted to the blades.

The blades were cleaned at the sensor application location. 3M double sided bonding tape (part # 927) was applied to the blade side of the sensors. The sensors were applied with force to the blades after the blade mounting area and the double sided tape were heated with a heat gun to increase tackiness. Gorilla brand duct tape was applied along the edges of the sensor. The double sided tape resisted out of plane forces and the duct tape resisted the shear forces being experience by the sensors to prevent detachment from the blades. The microphones and the accelerometers were installed together using predetermined pairs. Table 4.1 shows the microphone-accelerometer pairs. The final sensor setup can be seen in Figure 4.3. The sensors were installed onto the blades by working from the top of the nacelle. The installer was anchored into top the hub as shown in Figure 4.4.

Table 4.1 Sensor Naming and Pairing chart

Sensor Pairing Chart	
Accelerometer	Microphone
543 (Acc A)	A
648 (Acc B)	B
649 (Acc C)	C



Figure 4.3 Vibrational sensors mounted to the blade.



Figure 4.4 The installation from the top of the hub.

Each accelerometer was housed in a weatherproof PVC box (see blade mounting picture) with an extended life testing battery (90 day battery life) (See Figure 4.2). The contact microphones were mounted as is and required daily battery replacement. The main axis of the accelerometer was oriented with the length of the blade. The microphones' antennas were propped up off of the surface of the blades using a small plastic rod to enhance antenna communication with the receivers.

A compressed-air cannon, as shown in Figure 4.5, allowed for the ability to create strike events at the blades and perform system testing without damaging the blades. After evaluating different sports balls of various sizes and weights (e.g. American hand ball [~ 65 g and ~ 48 mm] and squash ball [~ 24 g and ~ 41 mm]), the launcher was barreled to shoot either a standard tennis ball (~ 57 g mass and ~ 67 mm diameter) or a tennis ball filled with water (~ 140 g mass) to represent some of the smallest birds and only twice the mass of the largest bat likely to be encountered. To simulate a strike event, the tennis balls were launched from the ground at about 10 m downwind to the rotor plane, shooting in an upwind direction. This provides two potential passes through the rotor swept area per launch when the wind velocity was sufficiently high - one pass traveling upwind and if not struck by a blade, then a second pass if the ball was blown back downwind traveling again through the rotor swept area. Due to fluctuating wind gusts and moving blades, the cannon's hit rate during field testing was low. Two tennis balls were loaded in series into the barrel and fired together, resulting in a higher hit rate. Tennis ball retrieval was an extensive and time consuming task [5].



Figure 4.5 Air cannon.

The wireless receivers (LORD MicroStrain 104-LXRS base station and Sun-Mechatronics UZ-10 UHF receiver), a NI USB-4431 DAQ and the triggering computer (see Figure 4.6 and Figure 4.7) were placed about 80 m upwind from the base of the tower. With this setup, each sensor's receiver was able to have a clear line of sight with the sensors, and we were able to monitor sensors' signals and to control when to initiate the recording of the system's signals. The recording for the sensors' signals were manually initiated and ended from the computer. A spotter relayed over two way radios when and where an impact occurred so the recording could be saved and the impact information recorded in the field notes.



Figure 4.6 Computer and wireless receivers setup in the field

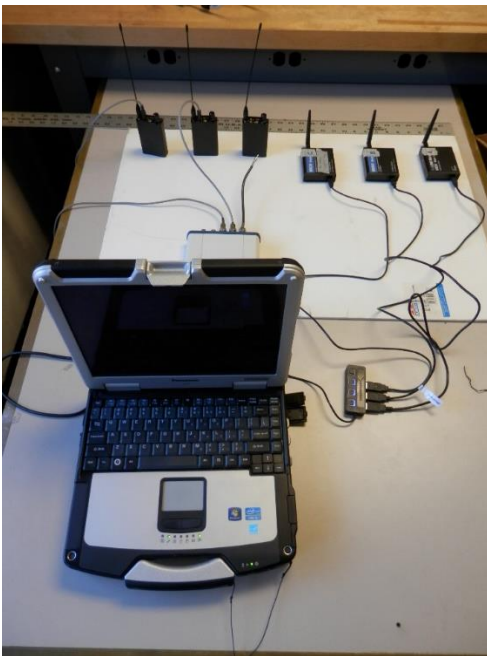


Figure 4.7 A reconstruction of the computer-receiver connections in the field

Extensive field notes were taken during the testing for proper post-testing documentation. The time duration into the recording at which the impact occurred was logged for post-processing, so the general location within the recording can be analyzed to identify the hit. The impact location on the 37 m blade was identified with three

distinctions: tip, middle, and root. It was recorded if the tennis balls were weighted or un-weighted with water. General operational details of the wind turbine were recorded such as blade speed, generator engagement, or wind turbine yawing. It was also noted if the tennis ball ricocheted off the blade and hit the tower. The impact location along leading edge, the chord of the blade, or the trailing edge was recorded when observed. The wind turbine's instrumentation readings for wind speed and direction as well as wind turbine's rpm, yaw and pitch position were collected from the facility's data base for the time periods that testing was occurring.

The camera testing that was completed at Mesalands was performed for the purpose of verifying the field of view simulations and the pixel size calculations (The field of view simulator is discussed in detail in section 4.2.2). Static images were taken at several positions from both the ground and the nacelle. Some of the image locations had been preselected using the simulator, but many locations were explored upon arrival. Figure 4.8 shows one of the locations that was selected before arrival to verify the simulator's results. The camera location with respect to the plane of the blades, the exposure, gain, focal length, aperture, and focus were all documented to help with image evaluation.

For cost savings and to demonstrate a proof of concept, the first-generation system will only cover a portion of the rotor swept area with cameras. For installation simplicity in initial field testing, the camera was mounted to the upper nacelle, with a field of view intersecting the rotor sweep area. A second position was evaluated from the ground with the camera in the rotor sweep area.



Figure 4.8 An evaluated camera location.



Figure 4.9 Taking images from the Nacelle.

4.1.3. NREL Field Testing

Testing at NREL occurred on the CART 3 [three bladed, Controls Advanced Research Turbine]. The CART 3 is a 600 KW turbine with 20 m blades and a 36.6 m tower [29]. For this field test all three sub systems, 1) the vibrational sensors and smart cameras, 2) the bioacoustic microphones, and 3) the optical camera node (Infrared and visual cameras), were test individually and as a system.

For testing, one wireless accelerometer and one wireless contact microphone was placed at the root of each CART 3 blade (Figure 4.10). Each accelerometer and each

contact microphone was housed in a weatherproof PVC box (see Figure 4.11) with either a 3 VDC (contact microphone) or 3.6 VDC (accelerometer) battery. The sensors' installation procedures at NREL 2 were the same as the ones used Mesalands except for installing occurred from a man lift instead of from the top of the wind turbine's hub as illustrated in Figure 4.12.



Figure 4.10 The microphone and the accelerometer mounted to the CART 3 blade.

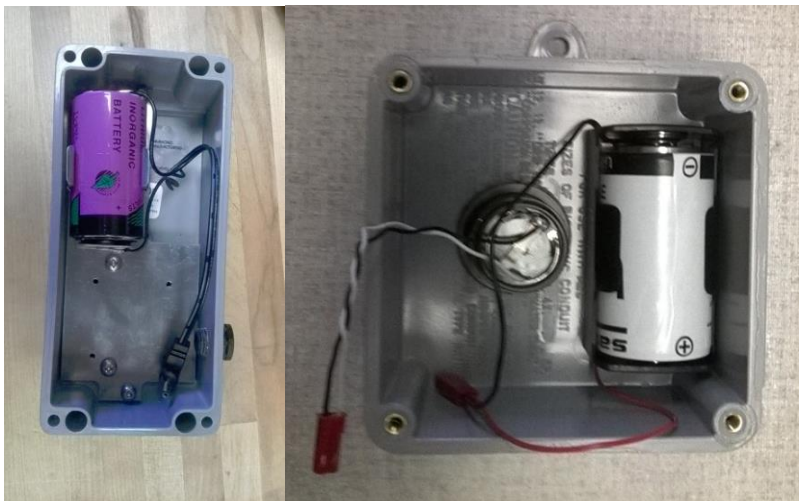


Figure 4.11 The accelerometer's (left) and the contact microphone's external battery boxes.



Figure 4.12 The sensors being installed onto the blades from a man lift.

The cameras at NREL 2 were positioned on the nacelle with the cameras looking down at the lower blade sweep quadrant and using a 12.5 mm focal length. No other testing location was tested. The smart cameras attached to tripods were mounted to the nacelle's safety cage.

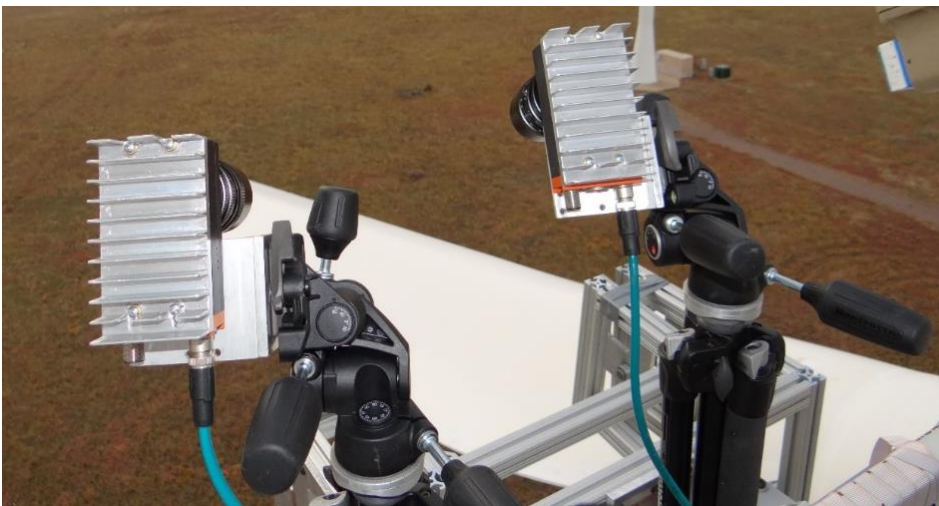


Figure 4.13 The smart cameras on top of the nacelle looking to the lower blade quadrant.

To save time in the field, a quick reference table was used to determine video capture time lengths for a given number of images and an exposure time (See Table 4.2).

To calculate the time shown in the interval between images column, add a .005 s buffer the exposure time column. This .005 s is an added safety processing time buffer. It was built into program for each image processed to allow time for complete image saving. A file size was calculated for a given number of images captured. This calculation was used to determine transfer time from the two smart cameras to the saving on the triggering computer and for setting the allotted memory for the ring buffer.

Table 4.2 Table of Image capture speed rate.

Exposure Time (s)	Interval Between Images (s)	Max Sampling Rate	Min Time Needed to Take 10 Images (s)	Min Time Needed to Take 15 Images (s)	Min Time Needed to Take 20 Images (s)
0.017	0.022	45.45	0.22	0.33	0.44
0.025	0.03	33.33	0.3	0.45	0.6
0.05	0.055	18.18	0.55	0.825	1.1
0.06	0.065	15.38	0.65	0.975	1.3
0.07	0.075	13.33	0.75	1.125	1.5
0.08	0.085	11.76	0.85	1.275	1.7
0.09	0.095	10.53	0.95	1.425	1.9
0.1	0.105	9.52	1.05	1.575	2.1
1	1.005	1.00	10.05	15.075	20.1

The air cannon served the same purpose for testing at NREL 2 as it did at Mesalands but it would operate from a new location, upwind from the wind turbine, because of safety concerns. The primary concern was that if the air cannon was fired from downwind a ball could ricochet back towards the operator at high velocities, giving little time to react. Firing from upwind only allowed for one pass of the tennis ball through the blade sweep area, decreasing the likelihood of creating an impact. Also for safety, all ball retrieval downwind occurred after the wind turbine was shutdown.

The main computer was placed inside the nacelle for close proximity to the cameras and receivers. The wireless receivers (LORD MicroStrain 104-LXRS base station and Sun-Mechatronics UZ-10 UHF receiver), and the NI USB-4431 DAQ were placed inside a weatherproof fiberglass box and were connected to the computer using a 5 m USB extension cord. With the receivers inside one box with an extension cord, it was easy to adjust the receiver's position. The receiver's mobility was necessary because before arrival, it was uncertain of the position with the best reception (at the front of the nacelle's roof or inside at the front of the nacelle). Figure 4.14 shows the weatherproof receiver case.

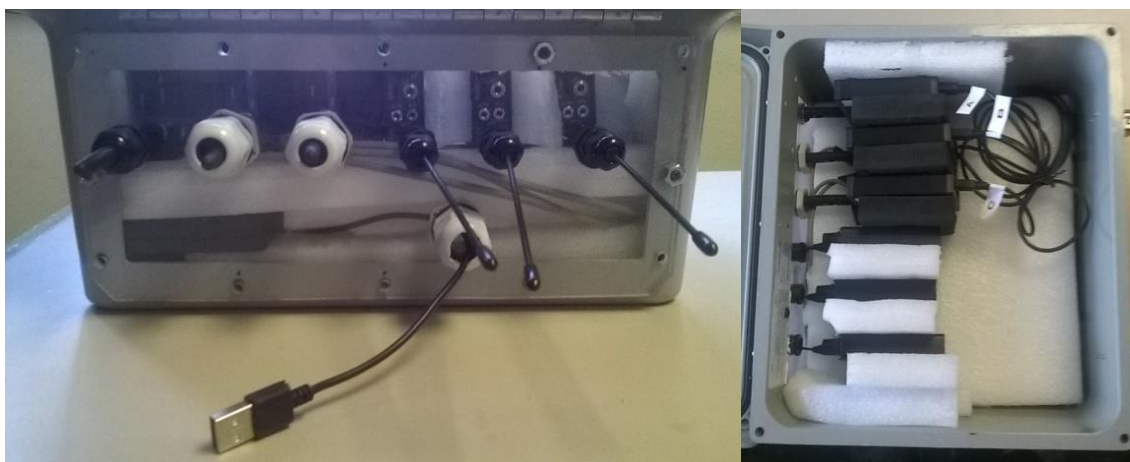


Figure 4.14 The front and the top view of the weatherproof receiver case for NREL 2.

The recording of the sensors' signals were manually initiated from the computer with automatic save initiation (The program has a user selected recording length). Using a remote desktop and a wireless access point to communicate with the main computer, the second computer on the ground would trigger the system when the wind turbine was in operation. The system was triggered from the nacelle if the wind turbine was braked. Like Mesalands, a spotter was used to relay over two way radios when and where an impact occurred. The recording would then be saved and the information documented in the field

notes. The same set of information that was recorded at Mesalands was also documented in the field notes at NREL.

4.1.4. Testing of the Camera Settings

With the limitations of the purchased technology, it was desired to find a camera placement where species identification could be performed on the resulting images for small to medium sized birds at a minimum. As shown in Figure 2.4, being able to distinguish between a marbled murrelet and cassin's auklet could be difficult depending on the camera's angle and the lighting that the image was taken. With Pacific Northwest bat species being small in size, as seen of the silver-haired bat's small wingspan in Figure 4.15, the objective of the cameras for the use of bats was to confirm the presents of a bat within the field of view, with the hope to have the ability to distinguish a bat from a small bird. Distinguishing between bat species would be unlikely. These limitations will continue to be less of a factor as camera technology continues to improve.



Figure 4.15 Silver-haired bat Wings extended.

The flight speed and the wing beat frequency, two related species characteristics, will determine the frame rate necessary for cameras to catch multiple images of the bird or bat for identification as it passes through the camera's field of view. "While target detection is likely to be possible over the entire blade span for the narrow field of view camera, spatial coverage is poor. Conversely, a lens that nominally provides a wider field of view is unlikely to allow target detection over more than half of the blade span" [5]. A smaller focal length would also help to determine the flight speed by allowing more frames of the animal to be captured within the field of view. Figure 4.16 illustrates this concept. If the bird is close the camera (position 1) then a wide field of view would be required to document the bird's flight speed; if the bird is at position 2, then either camera's field of view would record the flight speed. A minimum of two consecutive frames is need to

observe the flight speed, and the Nyquist frequency is the minimum frame rate needed to identify the bird’s wing beat frequency. Table 4.3 shows the correlation between field of view, frame rate, image resolution, observing the wingbeat frequency, and observing the flight speed. There is an inverse relationship between increasing the object’s resolution in an image, either through adjusting the camera’s image resolution setting or by narrowing the field of view, and the ability to discern the flight speed and wing beat frequency.

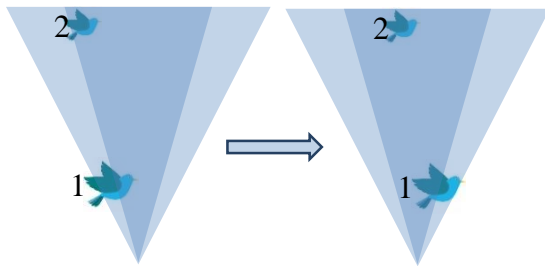


Figure 4.16 Two consecutive frames are illustrated to compare two fields of view and two bird distances from the camera.

Table 4.3 The correlation between camera settings and observing taxonomic information. P=Positive, N=Negative, No=No correlation.

		Constant				
		Observing the Flight Speed	Observing the Wingbeat Frequency	Image Resolution	Frame Rate	Field of View
Increasing	Observing the Flight Speed	No		P	P	P
	Observing the Wingbeat Frequency	No		P	P	P
	Image Resolution	P	P	N		N
	Frame Rate	P	P	N		No
	Field of View	P	P	N		No

Flight speeds for bird species of interest ranged from less than 2.7 m/s to greater than 26.0 m/s. Take the marbled murrelet and the short-tailed albatross, despite body size

differences, they can both fly up to speeds of 26 m/s. “Their morphology and flight behavior are also quite different with marbled murrelets being a diving species with small wings that typically fly close to the surface of the water, whereas albatrosses exhibit dynamic soaring during which they arc high above the water’s surface with large, extended wings, thereby influencing which part of the wind turbine structure each bird would most likely encounter” [5]. In comparison, A Silvered-haired bat can fly at speeds of 4.8 m/s. The range of the wing beat frequency for marine birds ranges from 3 Hz to upwards of 10 to 12 Hz.

The final consideration for camera placement was based upon these flight behaviors. Proposed camera locations were considered with the perspective of determining the camera position that would maximize the camera’s ability to record an event (pre-impact, impact, post-impact). If a heavy bodied diving bird impacted a wind turbine, it would impact the tower during diving or would be struck by a wind turbine blade in the lower quadrant of the blade sweep area. A dynamic soaring bird, if it was struck by a blade, would be flying through the upper quadrant of blade sweep area.

A collection of images were taken in Newport of sea birds. The focal point of each image was on a medium sized perched bird. Images were taken of birds at three known distances from the camera, 24 m, 57 m, and 102 m. Images were taken at various focal lengths, 18 mm, 22 mm, 30 mm, and 50 mm, for these distances. These distances are comparable with the 16.6 m (lowest point of the blade sweep area for CART 3), 36.6 m (CART 3 hub height), 43 m (lowest point in the blade sweep area for a 1.5 GE), 80 m (1.5 GE hub height) seen during the system field testing.

The three groups of images were evaluated to identify the minimum required focal length to perform species identification on the sea bird within the image for each respective distance. Because focal length has a linear relationship with image resolution, these distances and focal length values were linearly interpolated to create a general scale of the minimum required focal length at a given distance to perform species identification on a medium sized sea bird.

The three selected images from the three distances were then down sampled from 2592 x 1944 to half and quarter resolution. The down sampled images were then re-evaluated to determine if species identification could still be achieved.

4.2. Theoretical Methods

4.2.1. Field data examination

The first step in examining the field test data from Mesalands was to align the two sets of recordings created by the two separately triggered sensor programs. The process for manually triggering the programs created a discrepancy in the absolute start times of the recordings. Recordings from the program initiated first were truncated to align with the absolute start time of the recordings from the second sensor set.

Once the recordings were synced, a set of signal characteristics could be compiled into a quick reference table. This table was used to document the signal quality and future usefulness (e. g., triggering algorithms development) of the recordings from each test. The exact impact time, number of sensors observing the hit, general signal quality of the recording (especially around impact location), and impact signal strength were determined and listed in the table.

In order to determine the time of impact, signals were first visually inspected for a characteristic looking impact response at the estimated time of impact recorded in the field notes. If a characteristic impact response was found in one recording the remainder of the recordings were examined at the same time for a corresponding impact response. The total number of sensors that simultaneously observed the impact were chosen from the above examination process to determine the time of impact. Then an impact time was verified by examining the proximity of the proposed impact time to the estimated impact time recorded in the field notes. Once an impact time was determined, the total number of sensors observing the impact was logged.

An understanding of what the characteristic looking impact response was formed from examining the sensor responses to mallet and tennis ball hits on a static wind turbine blade; these signals are unmasked by operational noise. Figure 4.17 show a characteristic looking impact response from a mallet hit.

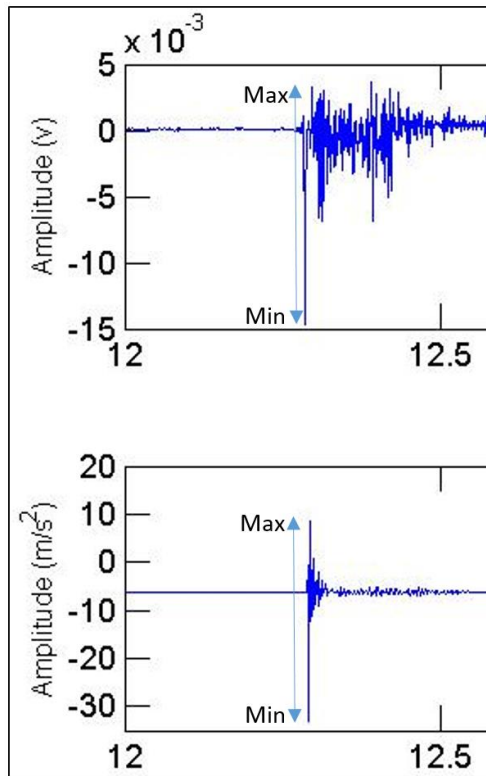


Figure 4.17 The impact amplitude calculation is illustrated on a blade mallet hit. Accelerometer (top) and microphone (bottom).

Next, the quality of the microphone and accelerometer recordings at the impact location was logged. These observations helped determine the validity of the proposed impact location. If the area around the impact location contained high noise, such as the false events in the microphone signal created by interference, the visual inspection was determined inconclusive and a final impact location was not logged. Lastly, the impact signal strength was determined and logged for each sensor that observed the impact.

The first step in determining impact signal strength was calculating the impact amplitude. The impact amplitude was calculated by subtracting the minimum value (point) within the characteristic looking impact response from the maximum value within the response region. Figure 4.17 illustrates the maximum and minimum points of an impact.

Second, the sensor's peak-to-peak amplitude was determined by calculating the standard deviation for a sampled section of the signal located in the vicinity of the impact. The standard deviation was then multiplied by four to determine the estimated signal amplitude. The multiplication factor was determined by assuming that the signal has a normal distribution, which gives 95.4% of the signal amplitude within plus or minus two standard deviations. As a result, the total estimated signal amplitude is four standard deviations. The remaining 4.6% of the signal thickness was assumed to be outliers and not included in the calculation. The impact signal strength (a percentage) of the signal could then be calculated by dividing the impact amplitude by the signal amplitude. For the accelerometer data an extra step was performed; the data was run through a high pass filter to eliminate the base sinusoidal wave before calculating the signal amplitude.

The impact signal strength was used to determine which of the three blades was hit. The impacted blade was identified by comparing the strength of the impact signal recorded by each sensor blade pair. If both the accelerometer's and the microphone's impact signal strength in a sensor pair were the largest among the sensor types, it was determined that the impact occurred on that blade. The sensor pair with the largest impact signal strength was selected (Table 4.4).

Table 4.4 An example hit of the six sensors' impact signal strength. Blade C was hit.

Hit Location	Impact % of Signal Magnitude Mic A	Impact % of Signal Magnitude Acc A	Impact % of Signal Magnitude Mic B	Impact % of Signal Magnitude Acc B	Impact % of Signal Magnitude Mic C	Impact % of Signal Magnitude Acc C
Tip	1008.025	255.7787	973.4155	205.2839	877.5999	653.6231

4.2.2. Image Pixel Simulator

Including daylight visual cameras in the sensor system was to fulfill two project requirements: 1) to obtain a visual confirmation of an event (or a missed event), and 2) to perform species identification. Appropriate camera placement, resolution adjustment, frame rate, and focal length will allow taxonomic information to be visualized in the recorded image sequence.

The driving consideration for the placement of visual cameras is to balance small enough pixel size for species identification with providing maximum allowable coverage of the blade sweep area. A quadrant of the blade sweep area was selected to show proof of concept. Three main mounting locations are being considered to cover the sweep area: 1) mounted to the tower looking up, approximately how cameras in the WT-Bird system was mounted, 2) mounted on the top of the nacelle looking up, and 3) mounted on the bottom of the nacelle looking down.

Once camera placement on the wind turbine has been selected, two factors need to be evaluated and adjusted, pixel size and depth of view. Determining the dimension of the largest pixel in a camera view will allow the user to determine whether there would be enough detail in the image for species identification and species distinction. Because of perspective distortion and lenses distortion, the resolution is not equal throughout the image. When the camera is on the nacelle and is in the plane of the blades looking radially out the camera lens will need a deep depth of view, from the root to the tip. When the camera is on the ground and is tilted up at the plane of the blades a large depth of view is

not needed. A simulation tool was developed to calculate an object's pixel resolution from a given camera distance, resolution and focal length.

Through the development of a series of MATLAB programs, the camera's placement performance was able to be predicted. With the development of a two dimensional field of view calculator, the camera's coverage of the blade sweep area for the in-plane camera placement can be modeled. With the development of a corresponding pixel size calculator, to determine the pixel size at the blade's furthest point seen in the camera's field of view.

“Determining the spatial resolution of an object (in number of pixels) at a given distance allows a user to determine the practical range for identification. Neglecting lens distortion, at a given distance (D) from the camera, the width (L) of the field of view is given as a function of the lens angle (θ) by the trigonometric relation $L = 2D \tan\left(\frac{\theta}{2}\right)$.

The size of a pixel at distance D is then given as L/R_x , where R_x is the horizontal resolution (i.e., 1296 pixels). The number of pixels spanning a target of interest, such as a marbled murrelet, can then be readily calculated on the basis of estimated body size. Target detection is unlikely to be possible if there are less than 3-4 pixels spanning a target” [5].

The simulator calculated the pixel size for a camera located on the ground or mounted to the tower looking up. To perform this calculation, the program required the hub height, blade radius, focal length, camera one and two Y axis placement and camera one and two pan angle. The program produced the field of view width and height angle and

camera one and two's max pixel size for the left and right spine of their field of view. For the example case in Figure 4.18, the program inputs are listed:

- Hub height: 80 m
- Blade radius: 40 m
- Focal length: 26 mm
- Camera 1 Y placement: 20 m
- Camera 2 Y placement: 20 m
- Camera 1 angle of tilt: 8°
- Camera 2 angle of tilt: -8°

For the camera input and output results, the X axis is perpendicular to the plane of the blades, the Y axis is both parallel to the plane of the blades and perpendicular to the tower, and the Z axis is perpendicular to the plane of the ground. For angle of pan, counterclockwise is the positive direction from a vertical orientation.

Figure 4.18 shows the bottom right quadrant of the blade sweep area will be mostly covered by the two cameras.

The example's output results are:

- FoV width angle: 12.64°

- FoV height angle: 9.43°

-Camera 1:

- Left spine max pixel size: $W=0.697$ cm, $H=0.692$ cm
- Right spine max pixel size: $W=0.676$ cm, $H=0.671$ cm

-Camera 2:

- Left spine max pixel size: $W=0.676$ cm, $H=0.671$ cm
- Right spine max pixel size: $W=0.497$ cm, $H=0.692$ cm

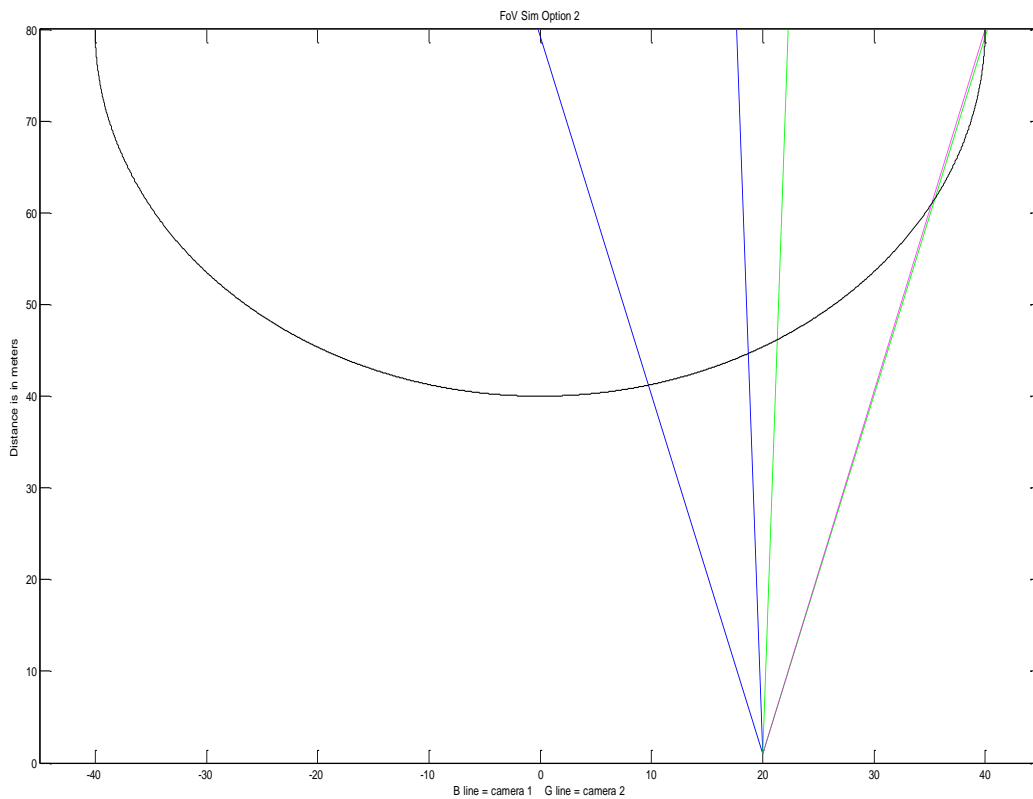


Figure 4.18 The coverage of the rotor blade sweep area by field of view captured by camera one (blue) and two (green).

4.2.3. Application of the Wavelet Algorithm

The first evaluated event detection method used was a floating analysis window for the fast Fourier transform (FFT). It was soon realized as Fugal states only a stationary signal or one that has a constant frequency is well suited for FFT. Wavelet analysis was then evaluated as an even detection method. Fugal also states a non-stationary signal or one that can change over time is well suited for wavelet analysis [30]. In order to make the impact event more clearly identifiable against the background vibrations (e.g., operational signal and noise), the raw signal data was processed using wavelet analysis as a noise reduction method. Verification of the feasibility to wavelet analysis on sensor signals as a filter to identify collision events was performed through the trial and error testing to identify the optimal wavelet. An optimized wavelet will detect events when they were visually undetectable. Figure 4.19 and Figure 4.20 show the microphone and the accelerometer recorded blade response, respectively, after a tennis ball hit. Below the signal, the corresponding wavelet analysis is shown. As can be observed in Figure 4.20, the high pass wavelet analysis works like a conventional high pass filter on the accelerometer signal.

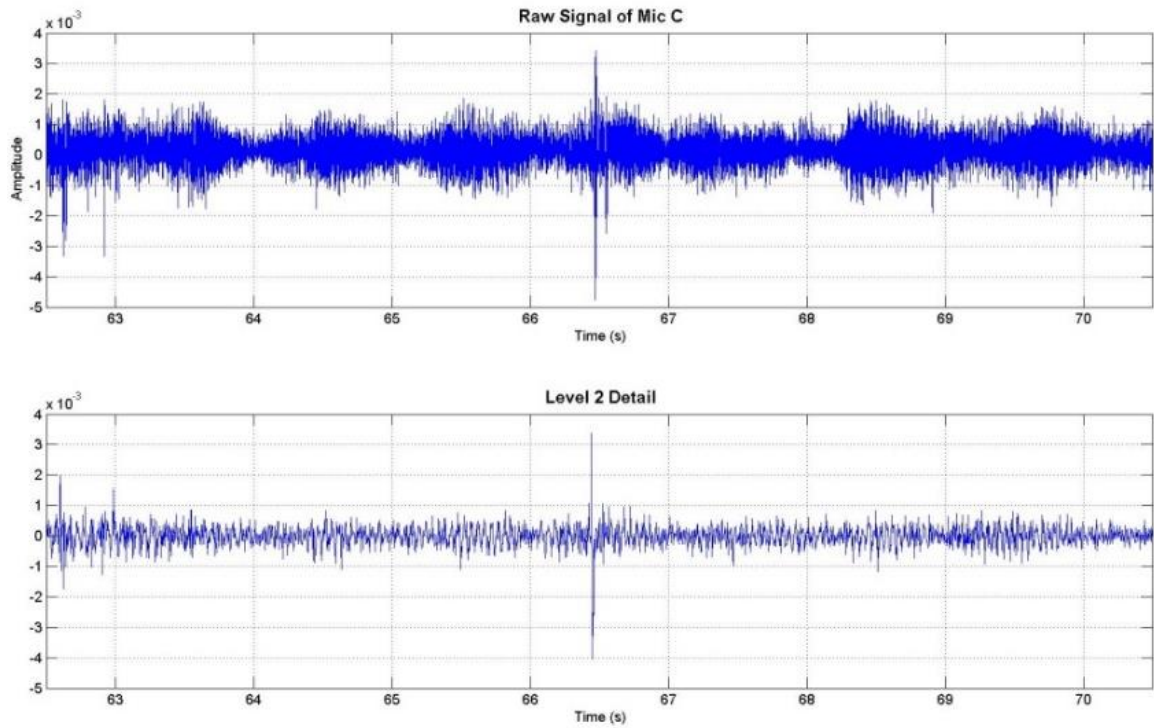


Figure 4.19 Raw signal and wavelet analysis for a microphone recording.

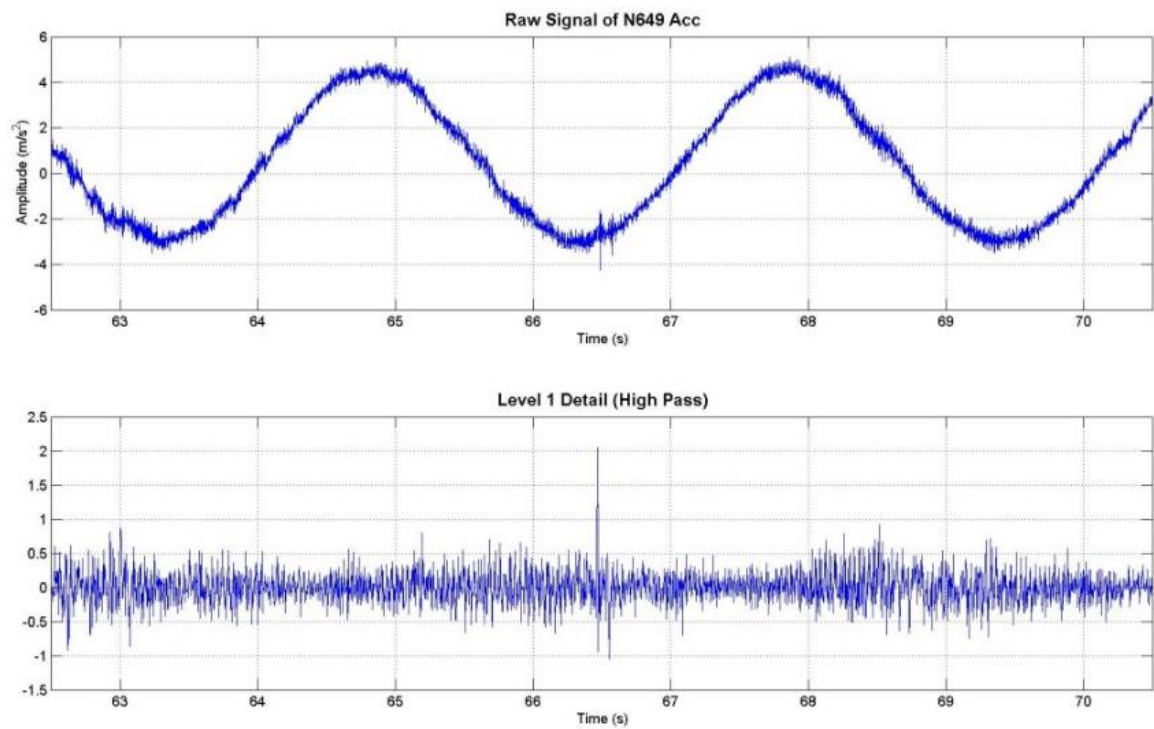


Figure 4.20 Raw signal and wavelet analysis for an accelerometer recording.

5. Field Tests Results and Discussion

This chapter examines the results from field testing at Mesalands and testing the camera settings at Newport. The specific results discussed from Mesalands will be the lessons from positioning the wireless sensors and receivers, the analysis of the vibrational sensors' recordings, and evaluation of camera positions.

5.1. Mesalands

5.1.1. Lessons from the Wireless Communication Design

After Mesalands, some interesting observations for event detection and sensor behavior were identified. "For both the accelerometer and microphone line of sight clarity to the receiver had a significant effect on wireless transmission range. During our testing, the wireless receiver was at ground level, 80 m from the sensors attached to the root of each of the three blades. Manufacturer's specified wireless transmission distance of digital accelerometer data was a maximum of 2 km line of sight with the use of the extended range setting. At 80 meters distance with the blade motion, we experienced some reception failure, especially at slow blade rotation speed, but fortunately the accelerometers were designed to store and resend data packets that were not successfully transmitted. We, therefore, experienced negligible accelerometer data loss. Manufacture specified wireless transmission distance of analog contact microphone data was shorter (80 - 150m line of sight) than accelerometers, appeared more affected by blade orientation, and did not store data packets for repeated transmission like that of digital data. However, under normal operation there was sufficient communication between wireless microphones and the receiver for accurate data collection. Unfortunately, the contact microphones flagged one

false event every second during certain wind conditions, which will require further algorithm development to prevent” [5]. Figure 5.1 shows a 90 seconds representative sequence of raw data collected from both sensors from the wind turbine operating under normal conditions. The accelerometer appears to be more affected by the facility operation conditions (e.g., blade position and speed); the intentional impact event was able to be visually identified on the time series plot. However, the contact microphone signal was obstructed by interference throughout the recording, as at the time of impact, making visual event identification infeasible.

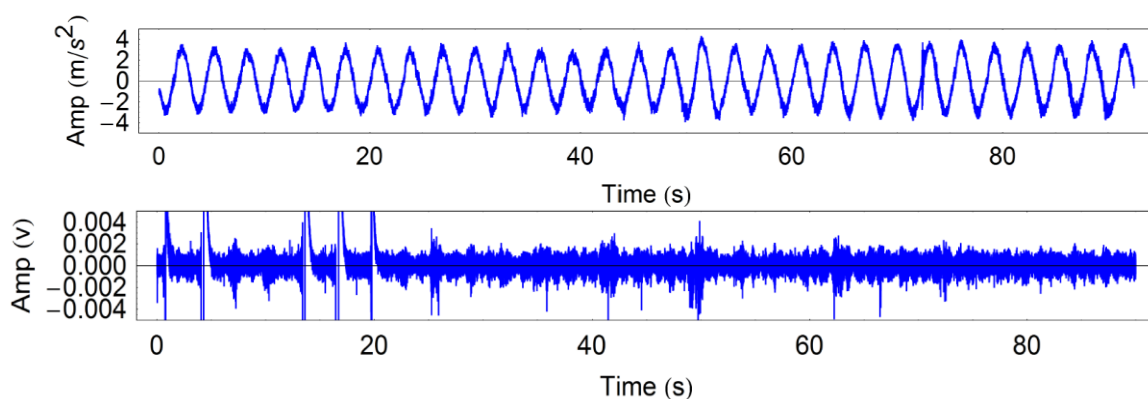


Figure 5.1 Raw signal plots from accelerometer (top) and contact microphone (bottom).

5.1.2. Vibrational Sensors

Although a volant’s mass does not contribute to species identification from the camera images it would influence sensor detection of a wind turbine collision. Table 2.1 shows the body mass range of the volant animals that the vibrational sensors needed to detect upon blade impact. Unlike “the impact kinetics with a fixed structure which is a function of mass and speed of the animal, the magnitude of an impact with a wind turbine blade will likely most often be a function of the animal mass and the blade speed (i.e., rpm and distance from the blade root) - it is more likely that a bird would be hit by the leading

edge of a blade than the animal running into the rapidly moving face of the blade (up to 250 km/hr or more). Therefore, during our experimental impact testing of the sensor array, we vary the mass of the object impacting the blade, but not the speed at which it is launched” [5].

Intentional impacts from tennis balls created strong observable events along the blade span, with impacts at the blade tip consistently producing strong signals. In addition to the recordings of simulated impacts, other tests were also performed to evaluate the sensitivity of the system. Impacts occurring on the tower could not be observed in the recordings when the wind turbine was in operation. After examining the recordings from the different operational situations, there appeared to be no concern for false positives. Figure 5.2 and Figure 5.3 shows the strong accelerometer signals generated by turbine startup and shutdown.

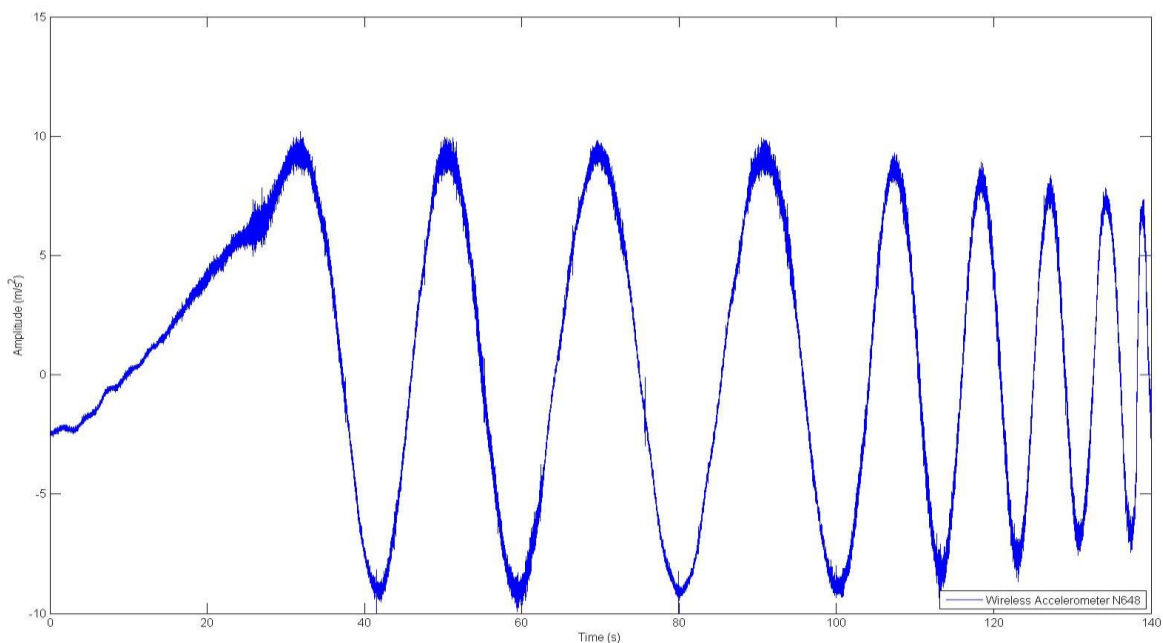


Figure 5.2 An accelerometer recording of a startup.

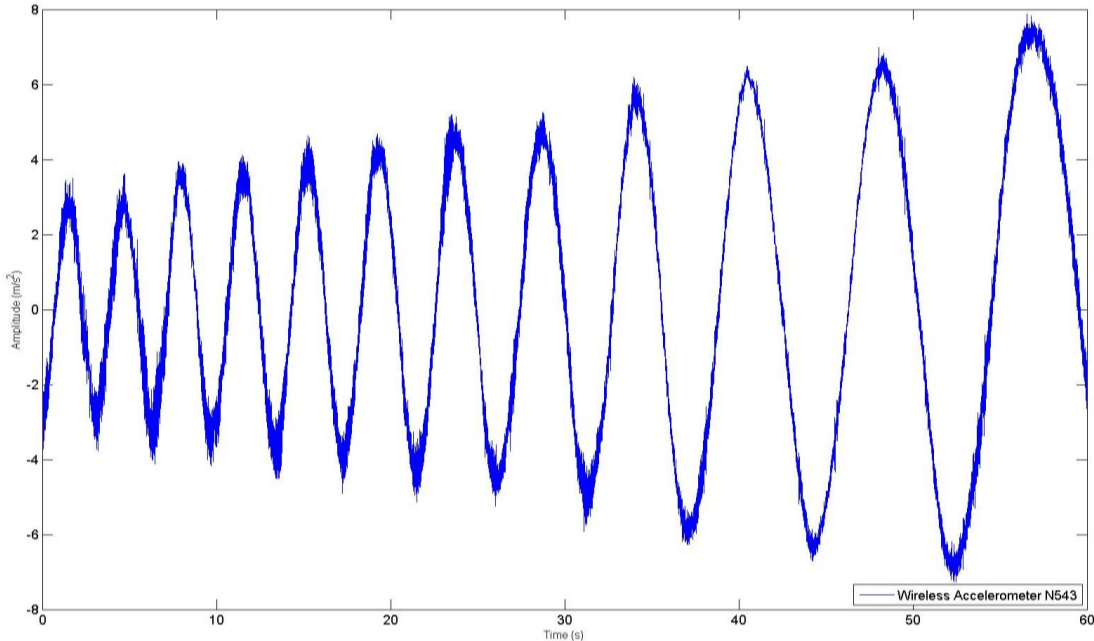


Figure 5.3 An accelerometer recording of a shutdown.

With the sensors on the blades and the wind turbine not in operation, recordings were taken of rubber mallet strikes on the nacelle as well as at the top and the bottom of the tower. Tapping on the side of the nacelle could not be observed by any of the sensors. Tapping at the top of the tower could be observed in all six sensors. Tapping at the bottom of the tower could not be detected by the sensors. This group of tests helped develop a more complete understanding of sensitivity of the system's sensors for various situations.

The rubber mallet strikes on the blade show the characteristic looking impact response and the length of time for the impact's resonance without background operational signal (See Figure 5.4). Figure 5.5 shows that if a simulated impact on one blade is strong enough, the impact will have enough energy to be detected by a sensor from any blade.

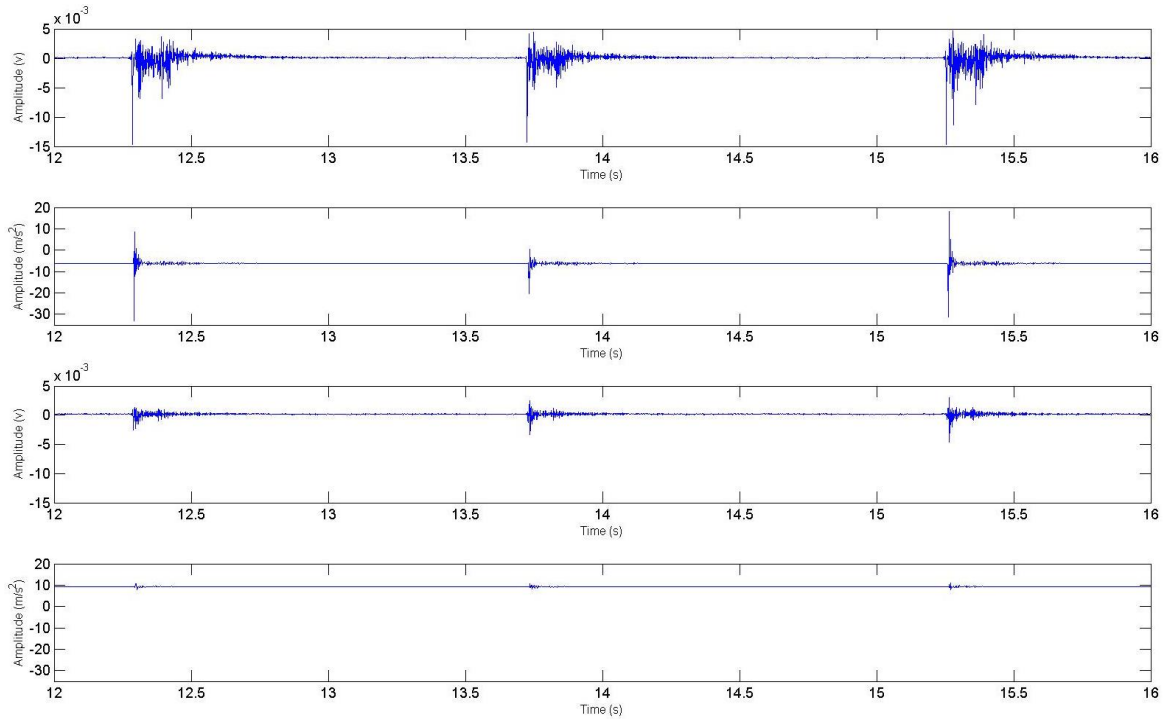


Figure 5.4 A blade mallet strikes with the observed response by the microphone (first) and the accelerometer (second) pair. A microphone (third) and accelerometer (fourth) response on a non-impacted blade.

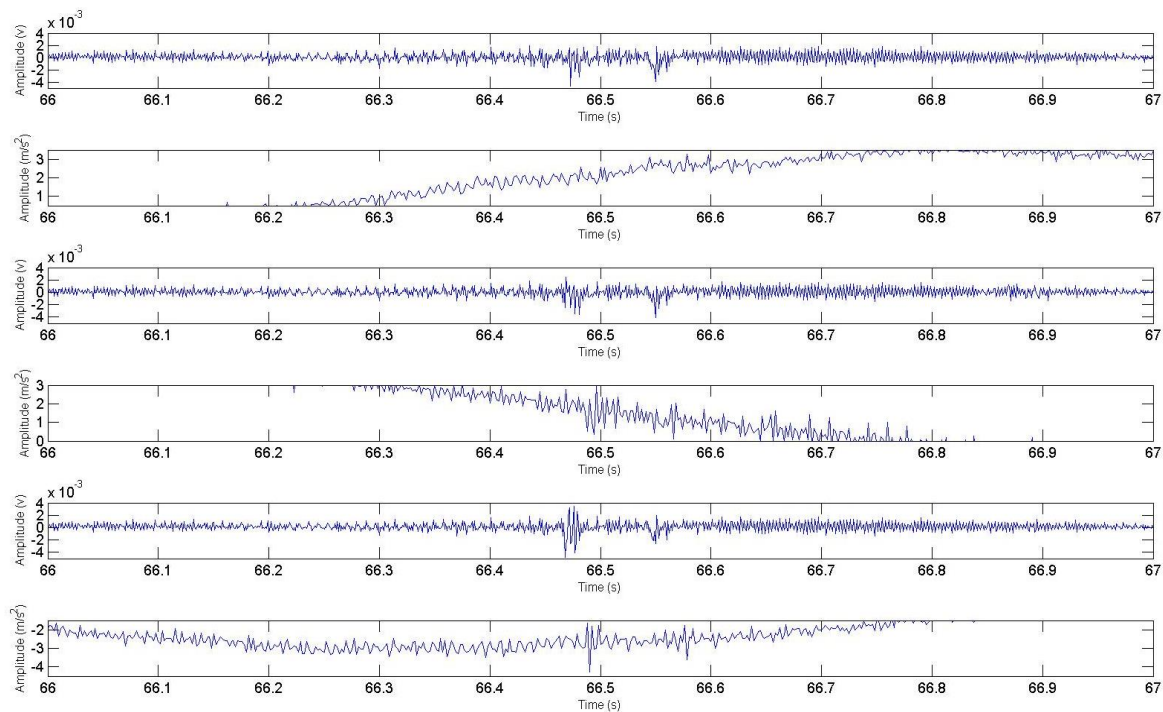


Figure 5.5 Measured reaction to a tennis ball impact for all three microphone-accelerometer pairs, Microphone (1st, 3rd, 5th), Accelerometer (2nd, 4th, 6th).

A total of 73 recordings were taken at Mesalands. 64 recordings were taken with the sensors on the wind turbine's blades. 22 operational noise recordings were taken of the wind turbine blades.

A total 33 hits were recorded including tower only hits, blade hits that ricocheted and hit the tower, and blade only hits; see Figure 5.6 for the location breakdown. The recordings from the blade only hits and blade-ricochet-tower hits were used for analysis. A total of twenty-three blade hits were recorded and used for analysis; 7 hits at the tip, 5 at the middle, 3 at the root, and 8 at an unknown location.

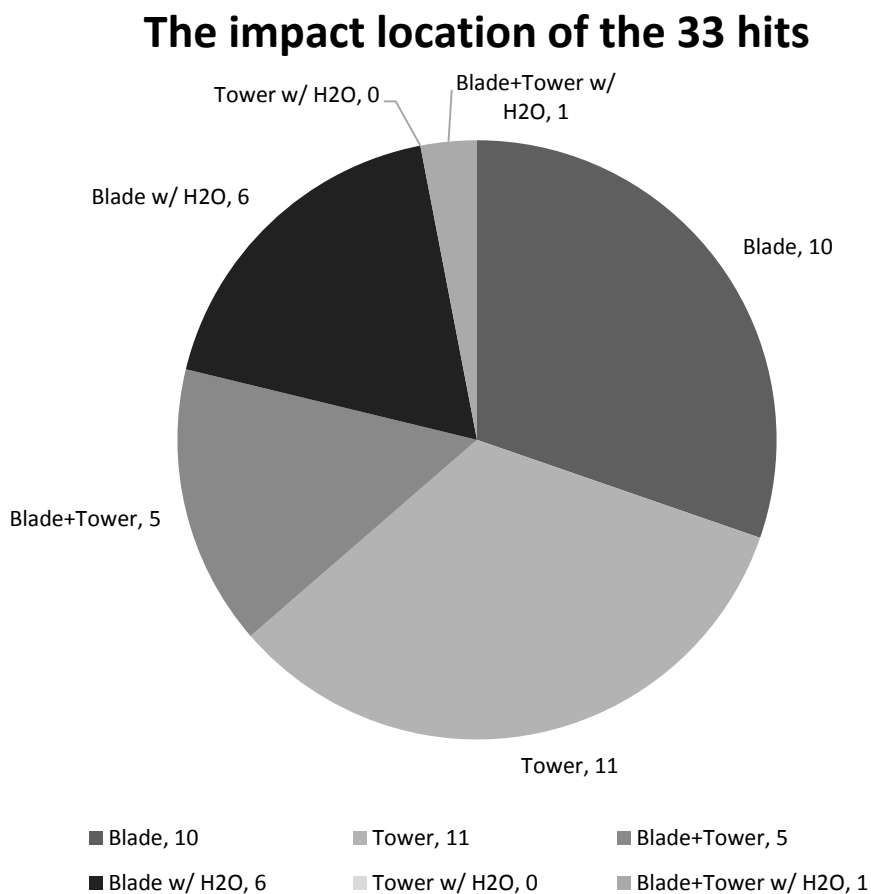


Figure 5.6 The location breakdown for the 33 tennis ball impacts.

Of the twenty-three blade impacts, thirteen were detected by at least one sensor through the visual inspection of the time history. Figure 5.7 shows the breakdown of the number of sensors detecting each simulated impact. Of the ten hits that were not observed, were 1 confirmed to have hit at the root, 1 middle, and 2 tip. This breakdown shows the significance of a detection algorithm that can identify an impact that is masked within the signal.

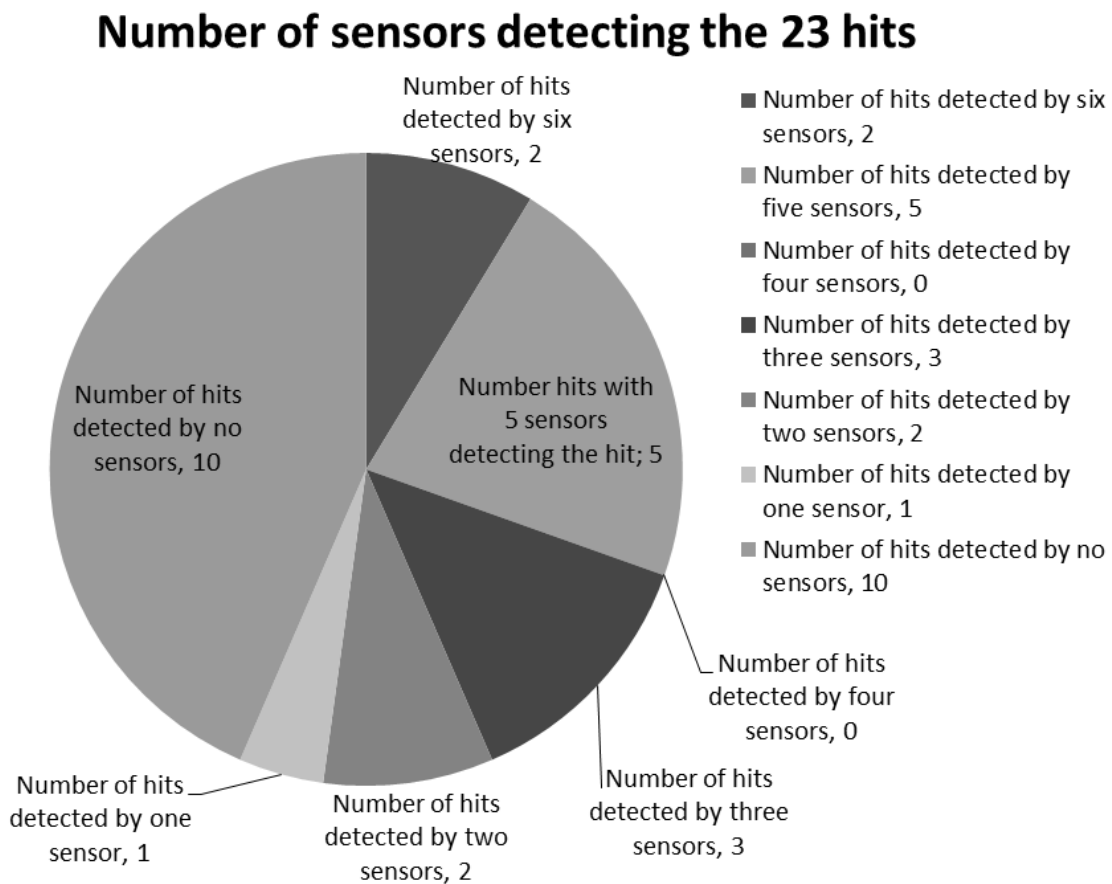


Figure 5.7 With one microphone and one accelerometer mounted to each of the three blades, the chart breaks down of how many of those sensors detected each simulated impact.

Examining the impact signal strength helped determine two questions: which blade was hit? and whether the tennis ball hit is a strong or a weak energy impact? For many hits

it was inconclusive in determining the impacted blade from comparing the pair's impact signal strength. The impacted blade could only be determined for 9 hits using this method. Using the hit location (tip, middle, root), weighted or un-weighted tennis balls, and the impact signal strength it could be determined if there was a correlation between these variables and the creation of a strong or weak energy impact. A strong energy impact could be detected in the majority of the sensors while a weak energy impact was only identified in less than half of the sensors. High energy impacts also consistently had high impact signal strength for the sensors.

The pre-field test hypothesis predicted a correlation between tennis ball mass and the hit location along the blade length with recorded impact signal strength. The predicted impact type with the largest signal strength was a weighted tennis ball impacting a blade tip. The predicted weakest was an un-weighted tennis ball impacting a blade root. However, no correlation was observed between the impact signal strength with the weighted and un-weighted tennis balls. The primary factor in determining the impact signal strength was hit location which is an indicator of impact velocity. The average impact signal strength for the tip was 646% for the microphone and 429% for the accelerometer for the 7 confirmed tip hits. For the middle, the average impact signal strength was 316% for the microphone and 320% for the accelerometer for 5 confirmed middle hits. For the root, the average impact signal strength was 376% for the microphone and 594% for the accelerometer for 3 confirmed root hits.

The impact signal strength results were examined to evaluate if a trend in sensor performance could be formed in order to answer some optimization questions: which is the

more sensitive sensor? and is it necessary to have sensors on each blade? If these two questions revealed clear answers, then it might be possible to reduce the number of blades needing to be monitored in the final system design. Potentially this analysis could also determine the better sensor for this application.

The idea of sensitivity for the comparison of the two sensors consisted of three parts: how many impacts each sensor type observed, how many sensors located on non-impacted blades observed the hit, and what was the average impact signal strength for each type of sensor.

Figure 5.8 shows that for two of the three blades the accelerometers sensed more hits. A total of twelve impacts were detected by the accelerometers. A total of eleven impacts were detected by the microphones. The difference between the total recordings and the number of hits each sensor detected is the number of undetected hits by the sensor.

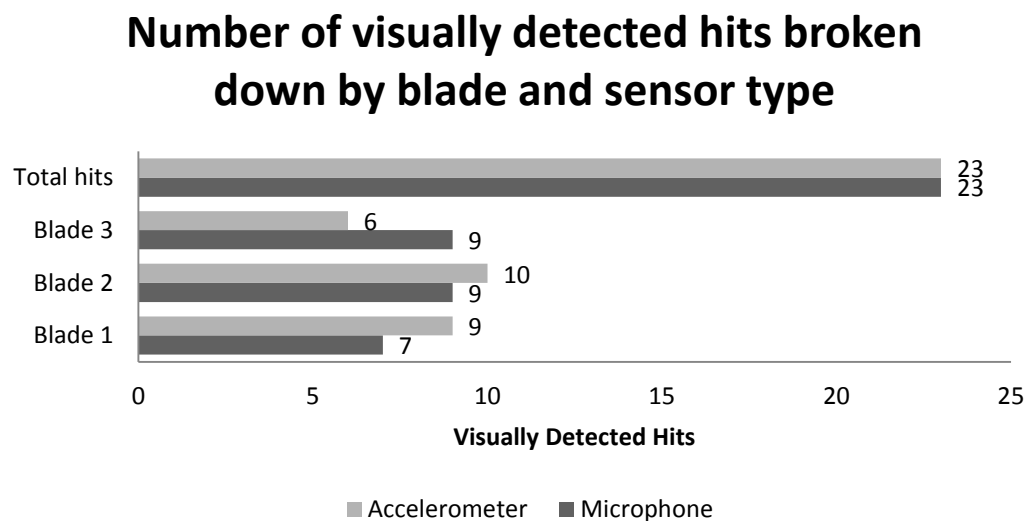


Figure 5.8 The number of visually detected impacts broken down by blade for each sensor type. A total of 23 impacts were recorded.

Figure 5.1 shows a breakdown of the number of sensors that visually detected an impact broken down by sensor type. From the below table and the figure, it was determined that the accelerometers were the more dependable sensor. If one accelerometer sensor detected an impact all the accelerometers were likely to detect it but at various magnitudes. Also a key finding from the data analysis is that 12 of the 69 impact locations (23 hits x 3 microphones) for microphone recordings were obstructed by interference or 17.4% of the recordings. This interference reduced both the number of total impacts that were detected as well as the number of blade impacts observed by the microphones on non-impacted blades.

Table 5.1 The number of sensors that visually detected each impact broken down by sensor type.

Sensor Type	Total Impacts Recorded	Number of Hits that 3 Sensors Detected	Number of Hits that 2 Sensors Detected	Number of Hits that 1 Sensor Detected	Number of Hits that No Sensors Detected
Accelerometers	23	5	4	3	11
Microphones	23	4	6	1	12

Comparing the impact signal strength of the accelerometer with the microphone, it was found that the three accelerometers' impact signal strength averages ranged from 368% to 453% of the signal strength. The microphones' impact signal strength averages ranged from 440% to 604%. This result demonstrates that the microphones produce a larger impact signal amplitude over the operational background noise. Consequently, microphones were more sensitive to observing false positives from the operational background noise. Because of these results, the microphones will require a finer tuned filter.

After comparing the observed sensor characteristics from the limited collected recordings, results were inconclusive in determining the better vibrational sensor for this application therefore, both sensors types will be intergraded into the system for future work. The results reveal that it will still be necessary to have both sensors on each blade because only thirteen of the twenty-three impacts were detected by at least one sensor.

5.1.3. Camera Placement

The expectations of the camera images were to evaluate the accuracy of the field of view simulator, as well as to select the camera placement for the system's second dynamic field test at NREL. Images from Figure 5.9 are from exploring locations for camera placement determined by the image pixel simulator. Figure 5.9 left is at the base of tower with a 12 mm focal length. Figure 5.9 right is an image taken on the ground 20m from the base of the tower and with a 26 mm focal length.



Figure 5.9 Two examples of the camera results from the ground.

The difference in required depth of view for species identification depending on the camera location can be observed in comparing the ground photos in Figure 5.9 with the

nacelle image in Figure 5.10. Figure 5.9 demonstrates when the camera is angled up at the plane of the blades a large depth of view is not needed (when the point of focus is of some distance from the camera e.g., from ground to hub). For the camera position in Figure 5.10, were the camera is in the plane of the blades looking radially out, the camera lens had to be adjusted to give a deep depth of view, from the tip to the root.

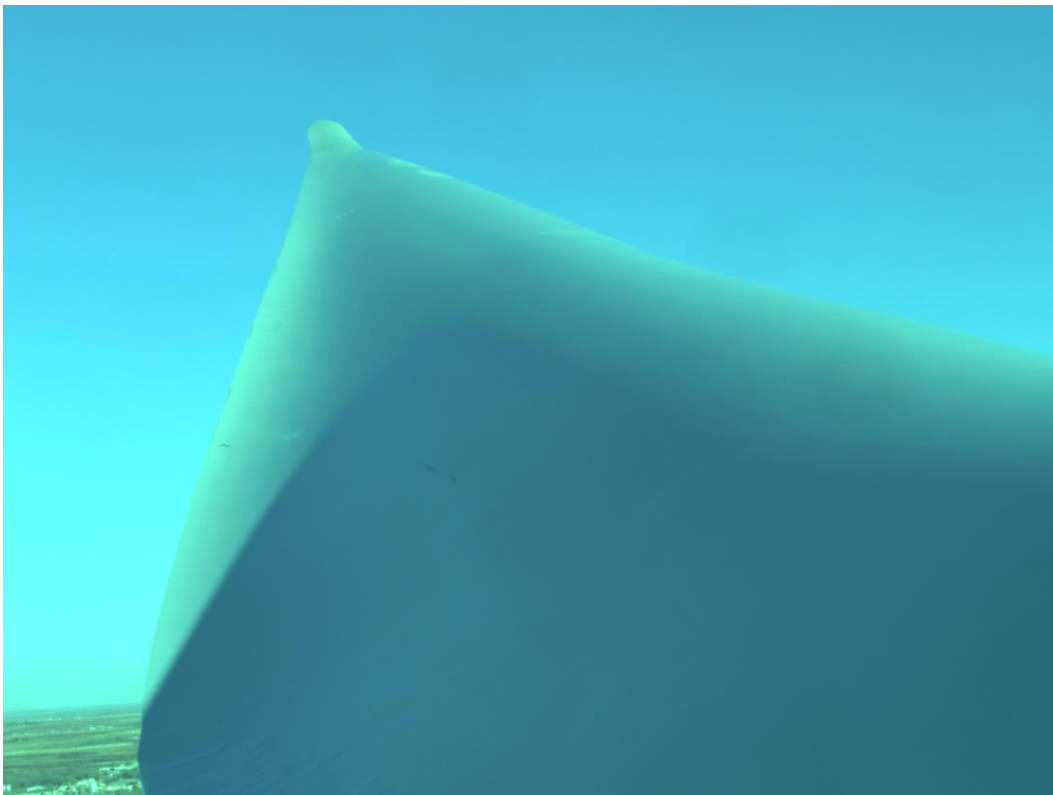


Figure 5.10 Camera on the nacelle looking up the blade length.

The right image in Figure 5.9 can be compared with the simulator results presented in Figure 4.18. The camera field of view in Figure 5.9 would be represented by camera 1 and the blue field view in Figure 4.18.

Further work will need to be completed in order to run a three dimensional field of view simulation such as for the camera's coverage shown in Figure 5.11, an image example

from a camera placed at the back of nacelle. This figure is an example of an image from an out of plane camera position.

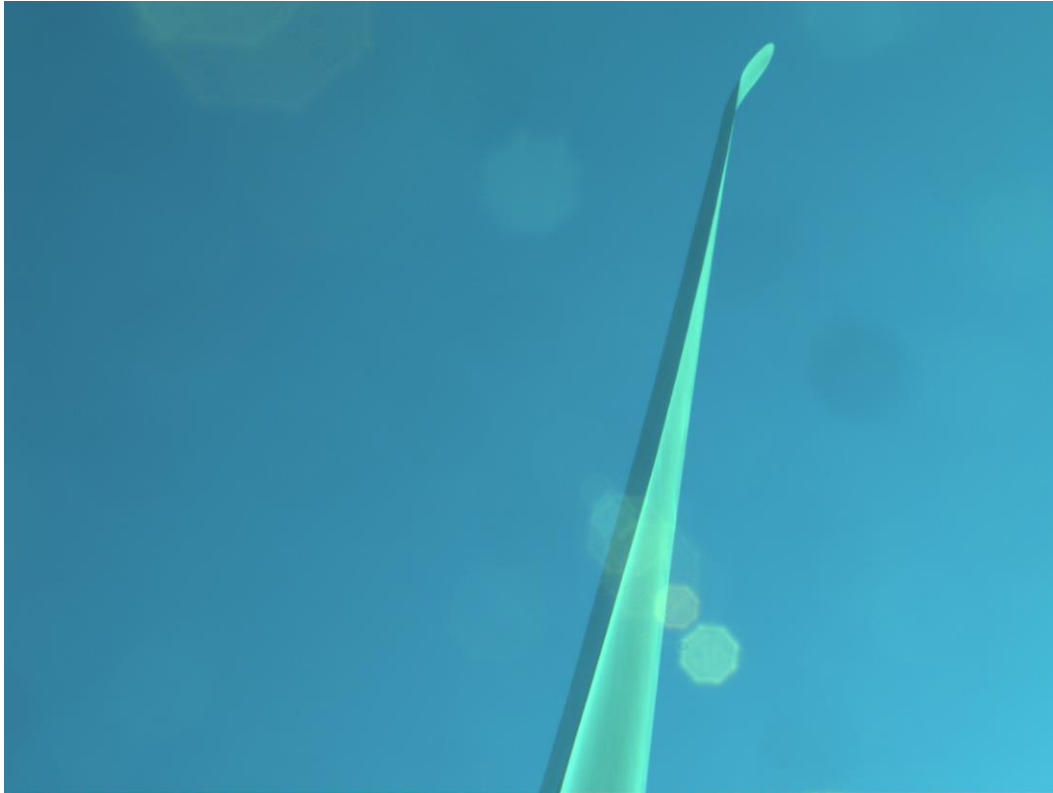


Figure 5.11 Camera at the back of the nacelle looking up at the blade tip.

5.2. Newport Image Evaluation for Camera Settings

The focal lengths of 30 mm, 22 mm, and 18 mm were found to be acceptable for species identification for the lengths of 102 m, 55 m and 24 m. Using these focal lengths a scale was produced for the minimum required focal length needed for a given distance to perform species identification on a medium sized sea bird. This scale gave a result of about ≈ 26 mm for the situation of focusing up at the 80 m hub height of 1.5 MW Turbine.

Figure 5.12 shows the 102 m image taken with 30 mm FL zoomed in on the focal point. Using Figure 5.13, the half resolution image, species identification was re-evaluated

to determine if the birds at the focal point were still able to be identified. A 1296 x 972 was recognized as still an acceptable camera resolution setting for the developed focal length scale. With the frame rate and the pixel resolution being linked, (See Table 5.2), this tradeoff of the down sampling the images allowed for an increased max frame rate of 45 Hz. The frame rate at 1296 x 972 is high enough capture the wing beat frequency for taxonomic purposes.



Figure 5.12 The 102 m image taken with 30 mm FL zoomed in on the focal point.



Figure 5.13 The half resolution image of Figure 5.12

Table 5.2 The Currera R linked max frame rate for a given resolution.

Currera R Max Settings			
Pixel Resolution	2592 x 1944	1296 x 972	648 x 486
Frame Rate (Hz)	15	45	80

6. Conclusions and Future Work

6.1. Conclusions

The purpose of this project was to develop an integrated detection system for remote monitoring of avian and bat interactions with offshore wind turbines. The proposed solution will reduce costs for environmental monitoring as well as mitigate or eliminate market barriers to the deployment of wind turbines. The multi-sensor instrumentation package includes vibration sensors, infrared and visual cameras and bioacoustic microphones networked together in an automatic event-triggered data acquisition system. The vibrational sensors were used to detect volant impacts with wind turbine blades. Infrared and visual cameras were included for event confirmation and species recognition. Bioacoustic microphones, an audio and an ultrasonic microphone, were used to monitor bird and bat presence, respectively, by detecting bird vocalization and bat echolocation. The system was field tested to evaluate each component's performance to detect simulated impacts and the efficacy of the system's integration.

An event count was logged with detectable hits identified using time histories from each vibrational sensor type to determine effectiveness. The accelerometer was shown to be the more reliable sensor in detecting hits. A novel analysis method was developed to quantify impact sensitivity for the vibrational sensors by dividing the impact amplitude by the signal amplitude (standard deviation of the signal) to give the impact signal strength (percentage). After performing this analysis on the collected recordings, the contact microphone was shown to be the more sensitive sensor due to its amplification of the impact over the signal strength. However, the microphone created more false positives than

the accelerometer from operational background noise. As a result, a finer-tuned filter is needed to identify between relevant events and false positives. Approximately 57 percent of the impacts were detected by the six sensors. However, only slight variations in sensor performance were found between the two sensor types. As a result, future work will continue to have both sensors on each blade to collect the data needed to determine the better sensor for this application.

Lens setting, image quality, and camera placement were tested and optimized for taxonomic classification. A scale was produced from field tests images for the minimum required focal length at a given distance to perform species identification on a medium sized sea bird. After performing down sampling on these images, a 1296 x 972 pixel resolution was recognized as an acceptable camera setting for a given focal length. Two appropriate camera positions were found: on the nacelle with the camera looking down at the lower blade sweep quadrant using a 12.5 mm focal length setting, and on the ground at the tower with the camera tilted up towards the blade tip using a 26 mm focal length setting.

The system's network design and software structure were developed to reduce network data saturation and the volume of data requiring post-processing or manual review. Event-based triggering along with ring buffers was used to address the problem associated with the conventional method of long-term camera and sensor deployment, the collection of large volumes of data requiring manual review.

During the field tests, several simulated impacts were recorded, proving the operability of the system. A library of these impact recordings was compiled for future

work in automatic detection algorithm development. When the cameras were triggered after a tennis ball blade strike, they successfully collected a sequence of images recording the event.

6.2.Future Work

Additional development and testing of the system's current software architecture needs to be performed in order to improve the system's robustness. Improvement upon the automatic detection algorithm will be necessary in order to perform an unattended long term deployment of the system. Weatherization of the sensors will also be necessary before long term deployment.

With the help of the project's advisory committee, the team has identified some missing elements of the system that would be necessary to improve the system's adaptability: active blade positioning and blade hit identification, sensor miniaturization, and reduction in the component's energy requirements, either through energy independence or increased energy consumption efficiency. The suggested applications for the sensor network included: assessing proposed facility sites, evaluating wildlife mortalities for existing wind facilities, integrating the system into the wind turbine during manufacture, and assessing efficacy of mitigation through active control of wind turbine operations or bird and bat deterrent technologies.

Bibliography

- [1] Lauha, F., Steve, S., Sgruti, S., and Limig, Q., 2012, “Global Wind Report Annual Market Update 2013,” Glob. Wind Energy Counc.
- [2] American Wind Energy Association, 2014, “U.S. Wind Industry Second Quarter 2014 Market Report Public Version,” AWEA Dep. Ind. Data Anal. Wash. DC.
- [3] Musial, W., and Ram, B., 2010, Large-scale offshore wind power in the United States: Assessment of opportunities and barriers, National Renewable Energy Laboratory (NREL), Golden, CO.
- [4] Kunz, T. H., Arnett, E. B., Cooper, B. M., Erickson, W. P., Larkin, R. P., Mabee, T., Morrison, M. L., Strickland, M., and Szewczak, J. M., 2007, “Assessing impacts of wind-energy development on nocturnally active birds and bats: a guidance document,” *J. Wildl. Manag.*, **71**(8), pp. 2449–2486.
- [5] Flowers, J., Albertani, R., Harrison, T., Polagye, B., and Suryan, R. M., 2014, “Design and Initial Component Tests of an integrated Avian and Bat Collision Detection System for Offshore Wind Turbines.”
- [6] Desholm, M., Fox, A., Beasley, P., and Kahlert, J., 2006, “Remote techniques for counting and estimating the number of bird–wind turbine collisions at sea: a review,” *Ibis*, **148**(s1), pp. 76–89.
- [7] Wiggelinkhuizen, E., Rademakers, L., Barhorst, S., and Den Boon, H., 2006, “Bird collision monitoring system for multi-megawatt wind turbines WT-Bird® Prototype development and testing.”
- [8] Verhoef, J. P., Westra, C. A., Eecen, P. J., Nijdam, R. J., and Korterink, H., 2003, “Development and first results of a bird impact detection system for wind turbines,” ECN Wind Energy, Madrid, Spain.
- [9] May, R., Hamre, Ø., Vang, R., and Nygård, T., 2012, “Evaluation of the DTBird video-system at the Smøla wind-power plant,” *Detect. Capab. Capturing -Turbine Avian Behav. NINA Rep.*, **910**.
- [10] “Bats - Smart and Transparent Wind Power - Automatic and Real-time Protection.”
- [11] Carbajo, R. S., Staino, A., Ryan, K. P., Basu, B., and Mc Goldrick, C., 2011, “Characterisation of Wireless Sensor Platforms for Vibration Monitoring of Wind Turbine Blades.”
- [12] Swartz, R. A., Lynch, J. P., Sweetman, B., Rolfes, R., and Zerbst, S., 2008, “Structural Monitoring of Wind Turbines using Wireless Sensor Networks,” *Smart Structures and Systems*, Cambridge.

- [13] Shump, K. A., and Shump, A. U., 1982, "Lasiurus cinereus," Mammalian Species, The American Society of Mammalogists, Northampton, MA, pp. 1–5.
- [14] Kunz, T. H., 1982, "Lasionycteris noctivagans," Mammalian Species, The American Society of Mammalogists, Northampton, MA, pp. 1–5.
- [15] Nelson, S. K., 1997, "Marbled Murrelet (*Brachyramphus marmoratus*)," The Birds of North America, Cornell Lab of Ornithology, Ithaca, NY.
- [16] Davis, W. B., and Schmidly, D. J., 1997, "Silver-haired Bat," The Mammals of Texas - Online Edition, Texas Tech University, Lubbock, TX.
- [17] Pierotti, R. J., and Annett, C. A., 1995, "Western Gull (*Larus occidentalis*)," The Birds of North America, Cornell Lab of Ornithology, Ithaca, NY.
- [18] Ainley, D., Manuwal, D. A., Adams, J., and Thoresen, A. C., 2011, "Cassin's Auklet (*Ptychoramphus aleuticus*)," The Birds of North America, Cornell Lab of Ornithology, Ithaca, NY.
- [19] Parker, N., 2003, COSEWIC Assessment and Status Report on the Short-tailed Albatross *Phoebastria albatrus* in Canada, COMMITTEE ON THE STATUS OF ENDANGERED WILDLIFE IN CANADA, Ottawa, ON.
- [20] Davis, W. B., and Schmidly, D. J., 1997, "Hoary Bat," The Mammals of Texas - Online Edition, Texas Tech University, Lubbock, TX.
- [21] Awkerman, J., Anderson, D., and Causey Whittow, G., 2009, "Laysan Albatross (*Phoebastria immutabilis*)," The Birds of North America, Cornell Lab of Ornithology, Ithaca, NY.
- [22] Briggs, K. T., Tyler, W. B., Lewis, D. B., and Carlson, D. R., 1987, Bird communities at sea off California: 1975 to 1983, Cooper Ornithological Society.
- [23] Suryan, R. M., Phillips, E. M., So, K., Zamon, J. E., Lowe, R. W., and Stephensen, S. W., 2012, "Marine bird colony and at-sea distributions along the Oregon coast: Implications for marine spatial planning and information gap analysis."
- [24] Jiang, Y., Tang, B., Qin, Y., and Liu, W., 2011, "Feature extraction method of wind turbine based on adaptive Morlet wavelet and SVD," *Renew. Energy*, **36**(8), pp. 2146–2153.
- [25] Graps, A., 1995, "An introduction to wavelets," *Comput. Sci. Eng. IEEE*, **2**(2), pp. 50–61.
- [26] Sung-Tae Park, and Jinguo Yang, 2004, "Engine knock detection based on wavelet transform," pp. 80–83 vol. 3.

- [27] Vetterli, M., and Herley, C., 1992, “Wavelets and filter banks: theory and design,” *Signal Process. IEEE Trans. On*, **40**(9), pp. 2207–2232.
- [28] Suryan, R. M., 2014, “Near Real-Time Detection of Avian and Bat Interactions with Wind Turbines.”
- [29] Fingersh, L. J., and Johnson, K. E., 2002, Controls advanced research turbine (CART) commissioning and baseline data collection, National Renewable Energy Laboratory.
- [30] Fugal, D. L., 2009, *Conceptual Wavelets in Digital Signal Processing: An In-depth, Practical Approach for the Non-mathematician*, Space & Signals Technical Pub.

